# Chapter 3 Spin-glass transitions in BF-xBT solid solutions

## 3.1. Introduction

Study of phase transitions in disordered magnetic systems has been a time honoured problem in the field of solid state and materials sciences [24,41–44]. In dilute magnetic systems (e.g. Cu-Mn), the ground state is known to be a spin glass (SG) state [24,42]. However, controversies still abound in the case of concentrated systems. Theoretically, it is known that the disordered concentrated magnetic systems can still lock into a long-range ordered (LRO) magnetic ground state if the disorder content (c) is less than a percolation threshold ($c_p$) for the exchange pathways, except that there is disorder induced broadening of the phase transition leading to the rounding of the susceptibility peak at the transition temperature ($T_c$) [24,195,244]. However, when the disorder content is close to the percolation threshold, the LRO percolative phase for both the Ising [238–241,245] and Heisenberg [242,243,246] systems has been reported to undergo another transition to the SG state. The pertinent questions that arise in relation to such systems are: (1) What is the true ground state? (2) Does the LRO phase coexist with SG phase in the ground state? (3) If both the phases do coexist, what is the proof that the SG phase has resulted from the same magnetic sublattice that led to the LRO phase? (4) Is the coexistence of SG phase with the LRO phase due to coexistence of isolated short range ordered (SRO) superparamagnetic (SPM) clusters with LRO clusters on two different magnetic sublattices as a result of segregation and clustering?

The theoretical treatments for such concentrated Ising as well as Heisenberg systems predict that the SG state can result from freezing of either the longitudinal or transverse components of the spin in the LRO phase and that it can coexist with the LRO phase on the same magnetic sublattice [49–53]. These theoretical predictions cannot be verified using macroscopic measurements (DC and AC susceptibilities) alone and require

microscopic tools (neutron scattering, Mössbauer spectroscopy etc.) which have been used for a few systems in support of the longitudinal/transverse freezing model in both the Ising and Heisenberg systems [238–243,245,246]. More interestingly, yet another interesting situation has been predicted theoretically for concentrated Heisenberg systems with small single ion anisotropy (D) as compared to the magnetic exchange interaction (J), where both the longitudinal and transverse components can freeze successively leading to two SG transitions below the so-called Almeida-Thouless (A-T) and Gabey-Toulose (G-T) lines, respectively [49–53]. Although most of these theoretical treatments are for concentrated ferromagnetic (FM) systems, these theories have been applied to disordered antiferromagnetic (AFM) systems as well [238]. While evidence for two SG transitions has been obtained in several systems using macroscopic measurements [247–250], the results are rather controversial as it is not clear if the LRO and the SG phases are formed on the same or separate magnetic sublattices. Unambiguous evidence confirming the occurrence of two SG transitions and coexistence of the two SG phases (SG1 and SG2) with the LRO phase on the same magnetic lattice using microscopic tools are rather sparse [e.g. Ref. [248]] in such systems.

Spin-glass phase has been reported in several multiferroic systems also [102,103,171,172,251]. Unlike the conventional SG systems, the multiferroic SG systems offer the possibility of verifying the theoretical predictions for concentrated systems through a study of the change in ferroelectric polarization and strain as a result of magnetoelectric and magnetoelastic couplings across the SG transition using diffraction techniques. A transition from LRO AFM phase to SG phase at low temperatures with coexistence of LRO and SG phases in the ground state has been reported in the multiferroic systems like pure [102,103] and disordered [251] $BiFeO_3$ and some site-disordered compounds like $Pb(Fe_{1/2}Nb_{1/2})O_3$ [171,172]. The origin of coexistence of SG

and LRO AFM phases at low temperatures in such multiferroics is still controversial as experimental evidences for and against both the phase segregation [171] and transverse freezing models [172] have been advanced in the literature. Further, there is no experimental report for LRO to LRO+SG1 to LRO+SG2 transitions in a disordered multiferroic systems. In this context, it is interesting to note that the single ion anisotropy (D) of $BiFeO_3$, a canonical Heisenberg system, is rather small as compared to exchange interaction (J) D/J ~0.00 [237] which falls within the range where two SG phases have been reported in non-multiferroic disordered systems like MgMn [52].

In this chapter, we present first experimental evidence in support of theoretical predictions for two SG phases below the A-T and G-T lines in coexistence with the LRO phase on the same magnetic sublattice in the multiferroic solid solution $(Bi_{1-x}Ba_x)(Fe_{1-x}Ti_x)O_3$ (BF-xBT) system using a combination of macroscopic (DC M(H,T), M(t), AC susceptibility ($\chi$ ($\omega$, T)) and specific heat ($C_p$)) and microscopic (x-ray and neutron scattering) measurements. We have selected $BaTiO_3$ based solid solution of $BiFeO_3$ for this study as it has received considerable attention in recent years due to large ferroelectric polarization [89,90,136], highest depolarization temperature for piezoelectric applications [136,140,144] and destruction of spin cycloid [87,89–91,93,143] leading to large remnant magnetization [87,89–91,93,143] as well linear magnetoelectric coupling [89,90]. From the analysis of neutron and x-ray diffraction data on BF-0.20BT, we demonstrate two distinguishing features of SG transitions in disordered multiferroics: (1) very strong and moderate magnetoelastic couplings associated with the SG1 and SG2 transitions, respectively, as revealed by the change in the unit cell volume ($\Delta V$) with respect to the theoretically predicted values, that scales quadratically with the spontaneous magnetization ($M_s^2$) and (2) strong magnetoelectric coupling at both the SG transitions as revealed by the large change in spontaneous polarization ($\Delta P_s$), calculated

from the atomic coordinates obtained by Rietveld refinements of the nuclear structure and the Born effective charges (BEC), at the two SG transitions. After presenting the results on BF-0.20BT, we also discuss the effect of dopant ($BaTiO_3$) concentration on the magnetic transitions in BF-xBT and construct a phase diagram showing all the magnetic phases.

### 3.2. Sample preparation:

Polycrystalline samples of $(Bi_{1-x}Ba_x)(Fe_{1-x}Ti_x)O_3$ (BF-xBT) solid solutions were synthesized by solid state route for x = 0.10 to 0.60 at $\Delta x = 0.10$ interval using high purity oxides of $Bi_2O_3$, $Fe_2O_3$, $BaCO_3$, $TiO_2$, $MnO_2$ (Aldrich and Alfa Aesar). The starting materials were carefully weighed in stoichiometric ratio and mixed in an agate mortar and pestle for 3 hours and then ball milled for 6 hours in acetone as mixing media using zirconia jar and zirconia ball. After drying, the mixture was calcined at optimized temperatures in the range 1073 K-1173 K depending upon the composition for 8 hours in open alumina crucible. The calcined powders were mixed with 0.3 wt % $MnO_2$ and ball milled again for 4 hours to break the agglomerates formed during calcination. $MnO_2$ doping reduces the leakage current as discussed in the literature [136–142,252] and also the previous chapter for $BiFeO_3$. We used 2 % polyvinyl alcohol as a binder to press the calcined powder into pellets of 12 mm diameter and 1 mm thickness at an optimized load of ~70 kN. After the binder burn-off at 773 K for 12 hours, sintering were carried out at optimized temperatures in the range 1173 to 1273 K, in closed alumina crucible with calcined powder of the same composition as spacer powder for preventing the loss of $Bi_2O_3$ during sintering. The sintering time was increased with increasing $BaTiO_3$ content from 1 hour for x = 0.10 to 4 hours for x = 0.60.

### 3.3. Characterizations:

The microstructure and chemical composition of the sample was obtained using Scanning Electron Microscope (SEM) (Zeiss, model no. EVO 18) and Energy Dispersive X-ray spectroscopy (EDX) attachment (Oxford, model no. 51-ADD0048). The sintered pellet was coated with conducting gold using sputter coater (Royal life Sciences, model no. DSR1) under vacuum before taking the SEM images. The composition analysis was also checked using Electron Probe Micro Analyzer (EPMA) (CAMECA SXFive instrument). The sintered pellet was coated with 20 nm thin layer of carbon using LEICA-EM ACE200 sputtering system. Natural silicate mineral andardite was used as internal standard to verify positions of crystals (SP1-PET, SP2-LiF and SP4-LPC0) with respect to corresponding wavelenght dispersive spectrometers in CAMECA SX-Five instrument. The following X-ray lines were used in the analyses: O-Kα, Ti-Kα, Mn-Kα, Fe-Kα, Ba-Lα & Bi-Mα. Natural mineral standards: hematite and pure metal standards (Mn & Bi) supplied by CAMECA-AMETEK were used for calibration and quantification. Routine calibration, acquisition, quantification and data processing were carried out using SxSAB version 6.1 and SX-Results softwares of CAMECA.

X-ray powder diffraction (XRD) measurements in the temperature range 12 K to 350 K were carried out using an 18-kW Cu rotating anode powder diffractometer (Rigaku, model no. RINT 2500/PC series) operating in the Bragg-Brentano geometry and fitted with a curved crystal monochromator in the diffraction beam. Sample environment was varied using a close cycle helium refrigerator based low temperature attachment on this diffractometer. The data in the 2θ range 20 to 120° were collected using annealed powders (10 hours at 773 K) obtained after crushing the sintered pellets at a step of 0.02 degrees.

High resolution synchrotron x-ray powder diffraction (SXRD) data were also collected at P02.1 beamline of PETRA III, Hamburg, Germany, at a wavelength of 0.2079Å (~60keV) for a few selected temperatures. The sample was filled in a quartz capillary of 0.8mm diameter. The temperature of the sample was adjusted by blowing a cold stream of $N_2$ gas produced by the Oxford CryoStream 700 cryocooler. At each temperature, the sample was exposed for 10 s by an incident beam with a cross section of 0.5 mm × 0.5 mm. Two-dimensional (2D) XRD pattern was recorded using a Perkin Elmer 1621 Detector (2048 pixels × 2048 pixels, 200μm × 200μm pixel size). The sample to detector distance was set to 1310 mm. The standard $LaB_6$ was used to calibrate the sample to detector distance. The 2D XRD pattern was integrated using the FIT2D software.

Temperature dependent neutron powder diffraction (NPD) data in the range 300 K to 2.8 K was collected at Druva reactor, BARC, Mumbai at a wavelength of 1.48 Å using high-resolution powder diffractometer PD-3. A close cycle helium refrigerator (CCR) (Cryogenic, A S Scientific UK) with variable temperature insert (VTI) was used for sample temperature variation. The powder sample was filled in a vanadium can of 6mm diameter and attached to the sample rod of the VTI. The nuclear and magnetic structures were refined by Rietveld techniques using FULLPROF suite [253].

DC magnetization (M(T, H)) measurements were carried out on a superconducting quantum interference device (SQUID) based magnetometer (Quantum Design, MPMS-3) in the temperature range 2 K to 900 K at 500 Oe applied dc field in two separate measurements from 2 to 400K and 300K to 900K range. The ac susceptibility ($\chi$ ($\omega$, T)) measurements were carried out in the temperature range 2 K to 300 K on the same machine using an ac drive field of 2 Oe.

### 3.4. Results and discussion:

#### 3.4.1 Microstructure and compositional analysis:

Fig. 3.1(a) depicts the scanning electron micrograph of BF-0.20BT solid solution. The average grain size of the ceramic sample obtained by linear intercept method is found to be ~2.5μm. The EDX spectra shown in the right panel reveal the presence of bismuth (Bi), iron (Fe), barium (Ba), titanium (Ti), manganese (Mn) and oxygen (O) atoms in our sample. The results of the quantitative analysis of the chemical composition of the atoms averaged over 10 different regions are given in Table 3.1. We have also confirmed the average composition of the ceramics through EPMA analysis, which gives the average composition more accurately. Results of average composition of Bi, Fe, Ba, Ti, Mn and O obtained by EPMA are given in Table 3.1. It is evident from the table that the values obtained by EDX and EPMA analysis are close to the expected (nominal) composition within the standard deviation except for the oxygen atom. Since, the accuracy of determining oxygen content is rather low due to its low atomic number, the average weight % of oxygen atoms can not be determined accurately from the EDX and EPMA.

Table 3.1: Quantification of BF-0.20BT by EDX and EPMA analysis

| Average Chemical Composition in Weight % | | | |
|---|---|---|---|
| | | EDX Analysis | EPMA Analysis |
| Element | Expected | Average | Average |
| Bi | 56.3 | 56.5 ± 1.8 | 56.2 ± 0.5 |
| Fe | 15.1 | 15.2 ± 2.3 | 15.0 ± 0.2 |
| Ba | 9.2 | 9.4 ± 1.4 | 8.9 ± 0.2 |
| Ti | 3.2 | 3.7 ± 0.9 | 3.1 ± 0.05 |
| Mn | 0.3 | 0.3 ± 0.1 | 0.22 ± 0.04 |
| O | 16.2 | 15.0 ± 2.2 | 15.2± 0.5 |

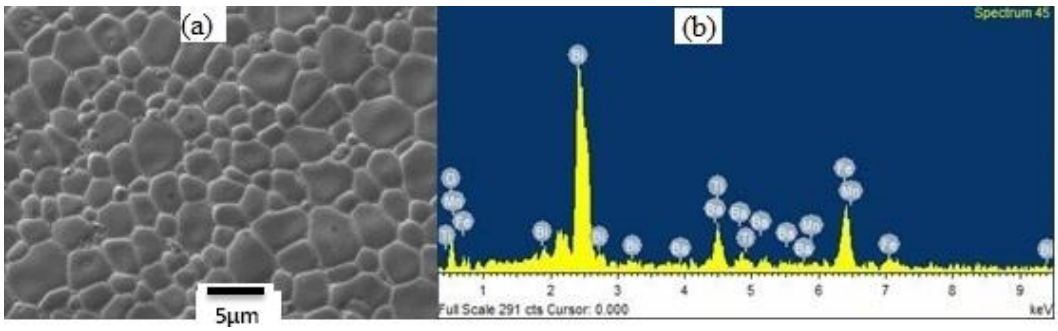


Figure 3.1: Left panel depicts the scanning electron micrograph of BF-0.20BT sample. Right panel show the EDX spectrum.

### 3.4.2 Room temperature crystal structure of BF-xBT:

Fig. 3.2 depicts the synchrotron x-ray diffraction (SXRD) patterns of sintered and well annealed powders of BF-xBT samples at room temperature over a limited 2θ range of 2.5-8.7 degrees for the composition (x) range $0.10 \leq x \leq 0.60$. It is evident from the figure that all the compositions exhibit pure perovskite peaks and no trace of any impurity phase is observed. This confirms that all the samples of BF-xBT correspond to a single phase. In order to study the room temperature crystal structure of BF-xBT samples as a function of composition qualitatively, we first plot the evolution of profiles of selected reflections $400_{pc}$, $440_{pc}$ and $444_{pc}$, (here all indices are with respect to a pseudocubic (pc) doubled perovskite cell) in the range $0.10 \leq x \leq 0.60$ in Fig. 3.3. It is evident from this figure that for the composition range $x \leq 0.30$, the $400_{pc}$ is a singlet, while $440_{pc}$ and $444_{pc}$ are doublets, which is expected for the stable rhombohedral structure of $BiFeO_3$ with R3c space group. It is also evident from the figure that the peak splitting of $440_{pc}$ and $444_{pc}$ pseudocubic reflections decreases with increasing x. This suggests that the rhombohedral distortion of $BiFeO_3$ gradually decreases with $BaTiO_3$ substitution. For the composition range $0.40 \leq x \leq 60$, all the peaks in Fig. 3.3 appear to be singlet which is a characteristic of a cubic-like phase with $Pm\bar{3}m$ space group. It is, however, known that these cubic-like compositions are not truly cubic as they possess local monoclinic distortion [91,135,145].

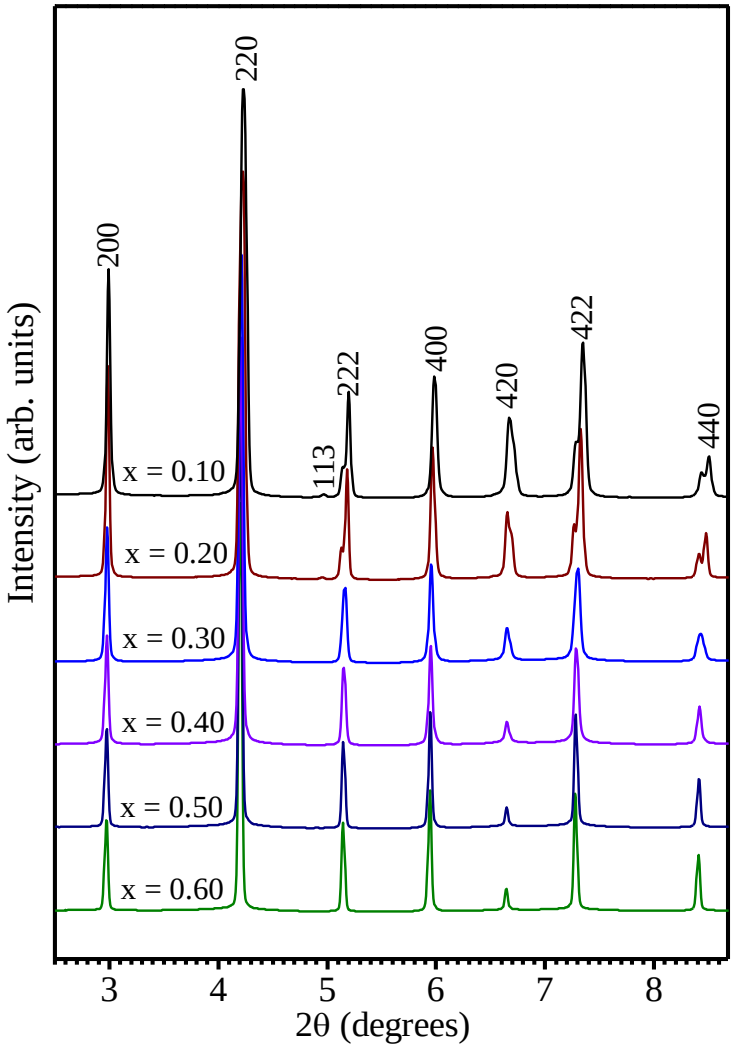


Figure 3.2: Synchrotron x-ray diffractogram of sintered and annealed powder of BF-xBT solid solutions for $0.10 \leq x \leq 0.60$. All indices are with respect to a pseudocubic (pc) doubled perovskite cell. The 113 reflection is a superlattice peak due to the anti-phase tilting of the oxygen octahedra about the trigonal $[111]_{pc}$ axis that doubles the unit cell size.

Thus, there are two different crystal structure regions corresponding to change of evolution of selected reflections $400_{pc}$, $440_{pc}$ and $444_{pc}$ of SXRD profiles.

In order to confirm the above qualitative observations, we have carried out Rietveld analysis of SXRD data using the FULLPROF package [253]. For the refinement of rhombohedral phase with R3c space group, we have used the atomic positions in

hexagonal cell given by Megaw and Darlington [254]. The coordinates of atoms in the asymmetric unit can be expressed as a function of displacement parameters s, t, d and e

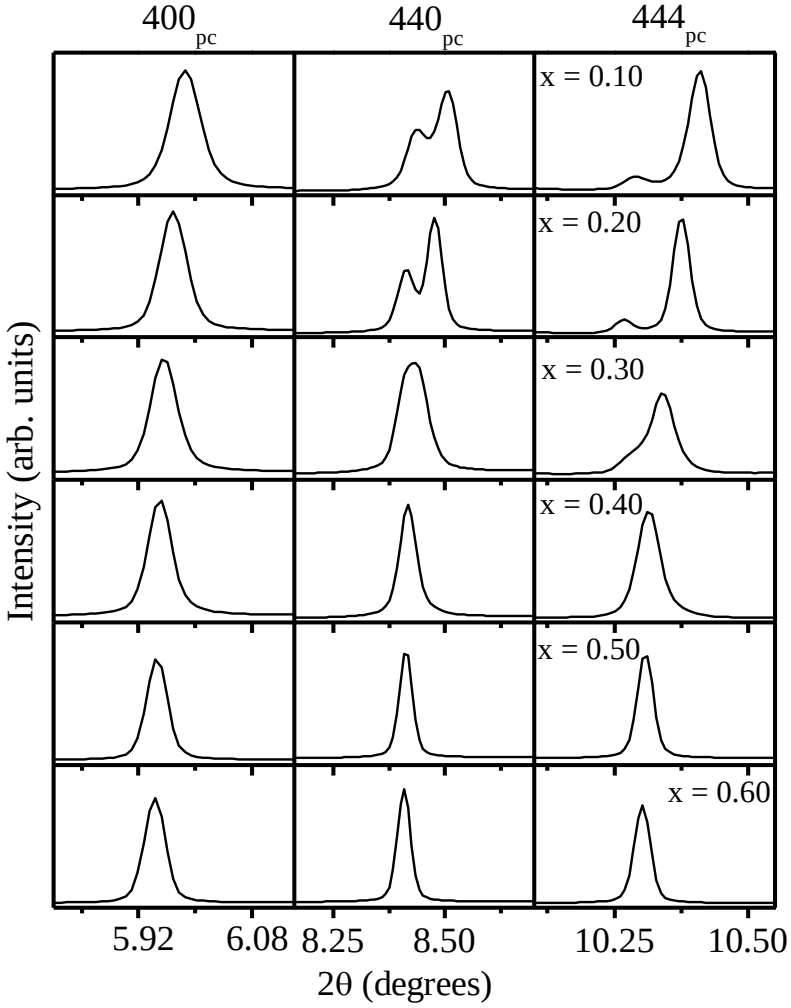


Figure 3.3: Composition evolution of selected profiles of $400_{pc}$,$440_{pc}$ and $444_{pc}$ reflection for BF-xBT in the composition range $0.10 \leq x \leq 0.60$.

as: $Bi^{3+}/Ba^{2+}$ (0,0,1/4+s), $Fe^{3+}/Ti^{4+}$ (0,0,t), $O^{2-}$ (1/6-2e-2d,1/3 -4d,1/12). The parameters 's' and 't' describe the polar displacement of cations $Bi^{3+}/Ba^{2+}$ and $Fe^{3+}/Ti^{4+}$ along $[111]_{pc}$ direction. The parameter 'e' gives the displacement of oxygen $O^{2-}$ from its ideal position and is related to tilt angle by the expression $\omega = \tan^{-1}(4e\sqrt{3})$ [254] whereas parameter 'd'

is related to the distortion of octahedra $BO_6$ (B: $Fe^{3+}/Ti^{4+}$) parallel to the $[111]_{pc}$ axis. The z coordinate of the oxygen atom was fixed and the remaining atomic positions were refined. The asymmetric unit of the cubic phase with $Pm\bar{3}m$ space group consists of three atoms: one A-site atom ($Bi^{3+}/Ba^{2+}$) at (0, 0, 0), B-site atom at (0.5, 0.5, 0.5) and one oxygen atom O at (0.5, 0.5, 0.0), respectively. All the atomic coordinates correspond to special positions in the cubic phase. Fig. 3.4 shows the observed (filled circles), calculated (continuous line) and difference (bottom line) profiles obtained after the Rietveld analysis of the SXRD patterns for selected compositions x = 0.20, 0.40, and 0.60 using space groups R3c, $Pm\bar{3}m$ and $Pm\bar{3}m$, respectively. Excellent fit between the observed and calculated profiles confirms the average crystal structures. In order to compare the unit cell parameters of rhombohedral and cubic phases as a composition, we have first calculated equivalent elementary perovskite cell parameters from the refined hexagonal 'c' and 'a' parameters of the rhombohedral phase for $x \leq 0.30$ using the following relationships: $a=a_H/\sqrt{2}$ and $c=c_H/2\sqrt{3}$. The variation of the elementary perovskite cell parameters for the composition range $0.10 \leq x \leq 0.60$, obtained from the Rietveld refinements, is shown in Fig. 3.5. It is evident from the figure that the structural phase boundary occurs around the composition $x_c = 0.40$ from rhombohedral (R3c space group) to cubic phase ($Pm\bar{3}m$ space group). The unit cell volume (see Fig. 3.5 (b)) shows a change of slope across the structural phase boundary. The observed structural phase boundary is in agreement with the previous reports [90,91]. The refined structural parameters for all compositions of BF-xBT are given in Table 3.2.

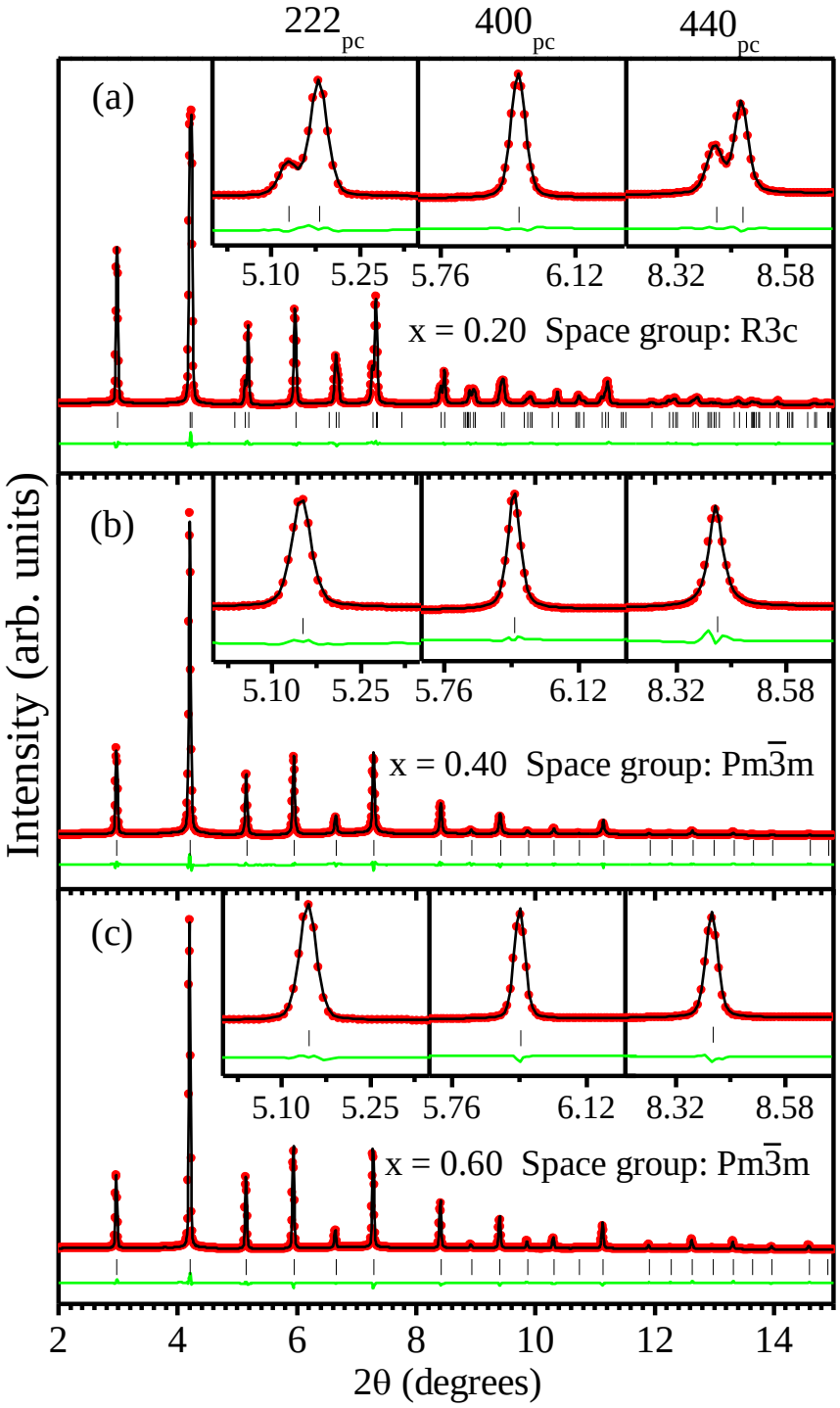


Figure 3.4: Rietveld refinement using synchrotron x-ray diffractogram of (1-x)$BiFeO_3$-x$BaTiO_3$ powders for representative compositions x = 0.20, 0.40, 0.60 using **(a)** Rhombohedral R3c space group **(b)** Cubic $Pm\bar{3}m$ space group and **(c)** Cubic $Pm\bar{3}m$ space group. Inset depicts the fits for the pseudocubic reflections $222_{pc}$, $400_{pc}$ and $440_{pc}$.

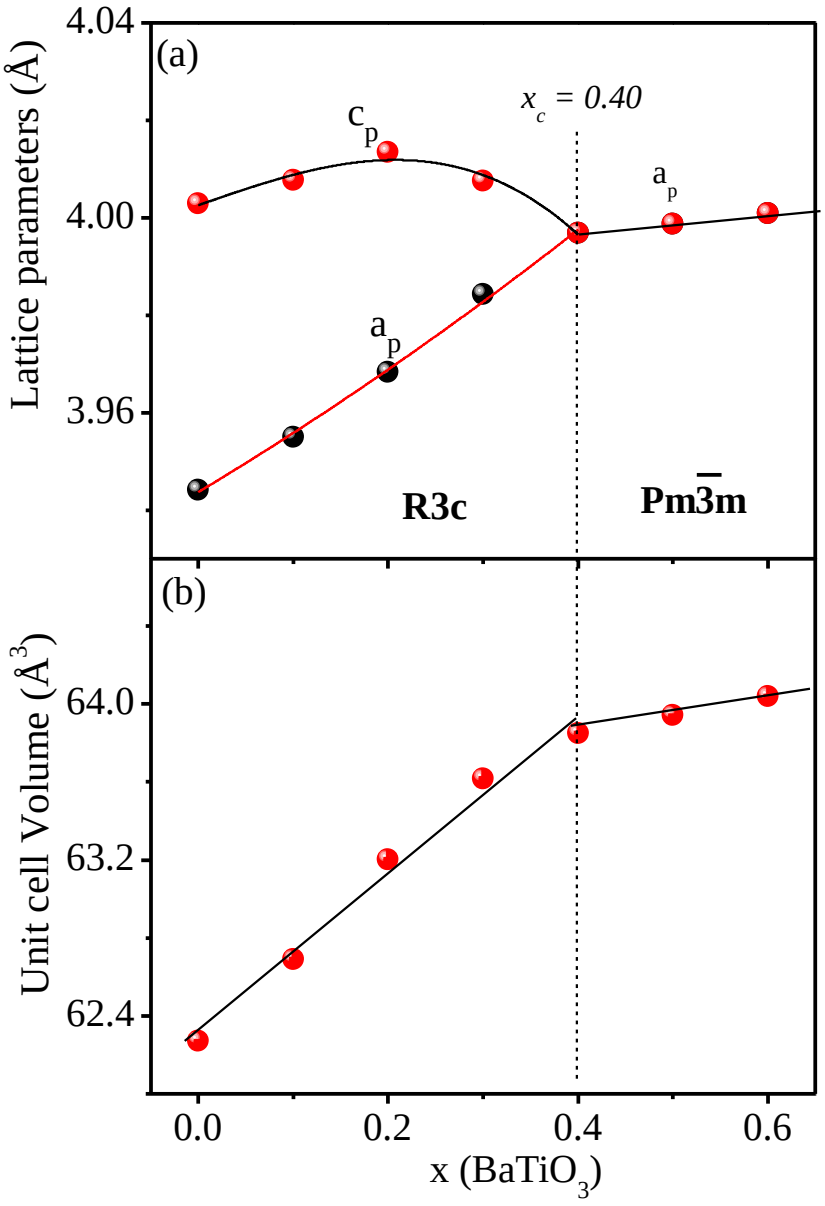


Figure 3.5: Variation of elementary perovskite (a) cell parameters (b) unit cell volume of BF-xBT as a function of composition (x) at room temperature. The structural parameters for x = 0.0 i.e. $BiFeO_3$ was taken from the previous chapter's analysis.

Table 3.2: Refined structural parameters for various compositions of BF-xBT (for $0.10 \leq x \leq 0.60$)

| x | 0.10 | 0.20 | 0.30 | 0.40 | 0.50 | 0.60 |
|---|---|---|---|---|---|---|
| Space group | R3c<br>$a = b \neq c$, $\alpha = \beta = 90^0$, $\gamma = 120^0$ | | | $Pm\bar{3}m$<br>$a = b = c$, $\alpha = \beta = \gamma = 90^0$ | | |
| a(Å) | 5.5932 (8) | 5.6125 (3) | 5.6346 (5) | 3.9968(5) | 3.9987 (1) | 4.0008 (9) |
| c(Å) | 13.8691 (5) | 13.9016 (6) | 13.8828 (4) | - | - | - |
| Bi (z) | 0.2952 (6) | 0.2889 (6) | 0.2668 (9) | 0 | 0 | 0.5 |
| Fe/Ti (z) | 0.0189 (6) | 0.0146(6) | 0.0996 8) | 0.5 | 0.5 | 0.5 |
| O (x) | 0.2285 (2) | 0.2030 (8) | 0.1873 (1) | 0.5 | 0.5 | 0.5 |
| O(y) | 0.3506 (2) | 0.3405 (3) | 0.336 (2) | 0.5 | 0.5 | 0.5 |
| B(Bi/Ba) | 1.03 (2) | $\beta_{11}$= 0.0242(3)<br>$\beta_{33}$=0.0035(1)<br>$B_{eq}$=3.44 | $\beta_{11}$= 0.041(7)<br>$\beta_{33}$=0.007(2)<br>$B_{eq}$=5.9 | 4.99(1) | 4.51(4) | 4.47 (4) |
| B (Fe/Ti) | 0.43 (6) | 1.19 (9) | 1.1 (1) | 1.54 (6) | 1.26 (5) | 0.85 (4) |
| B(O) | 1.15 (2) | 3.8 (3) | 5.1 (5) | 4.26 (1) | 2.6 (2) | 1.7 (1) |
| $R_{wp\,(\%)}$ | 8.14 | 9.26 | 10.8 | 9.92 | 9.73 | 9.41 |
| $R_{p\,(\%)}$ | 7.68 | 8.97 | 9.91 | 8.65 | 7.62 | 8.69 |

### 3.4.3 Magnetic transitions in BF-0.20BT:

#### 3.4.3.1 The Néel transition:

The antiferromagnetic (AFM) Néel transition in pure $BiFeO_3$ (BF) occurs at $T_N$ ~650K. As a result of 20% substitution of $BaTiO_3$ in BF, i.e. in BF-0.20BT, $T_N$ decreases due to dilution of the magnetic sublattice. Fig. 3.6 depicts the variation of DC magnetization (M(T)) with temperature on a zero-field cooled (ZFC) sample of BF-0.20BT recorded during sample worming under an applied field of 500 Oe in the temperature range 300 to 900K. It is evident from the figure that a long-range ordered (LRO) magnetic phase emerges below $T_N$ ~608K in agreement with the previous reports [91]. The nature of ZFC M(T) response of BF-0.20BT is, however, not like a typical AFM transition seen in pure BF but is rather like a ferromagnetic (FM) transition.

The FM type transition is due to the destruction of the spin cycloid, superimposed on the canted G-type AFM arrangement of spins in BF, that releases the latent FM component of the spins in the magnetic sublattice. This was confirmed through M-H hysteresis loop measurements, Curie-Weiss plot and neutron diffraction patterns.

The M-H hysteresis loop of BF-0.20BT is shown in Fig. 3.7. It reveals weakly ferromagnetic behaviour (see Fig. 3.7) in contrast to linear M-H characteristic of AFM phase in pure BF. However, even in pure BF, the M-H loop opens up with a remanant magnetization $M_r \sim 0.3$ emu/g at 10 K on destruction of the spin cycloid in the presence of external magnetic field in excess of ~20T [84]. The opening of the hysteresis loop in BF-0.20BT even at moderate fields thus indicates the destruction of the spin cycloid of $BiFeO_3$ as noted by previous workers also in various solid solutions of BF [91–93,143]. The remanant magnetization $M_r \approx 0.13$ emu/g of our samples is close to the value of ~0.15 emu/g reported by Singh et al. [91]. The fact that the magnetization does not saturate even at 7T field clearly suggests weakly FM behaviour due to canted AFM structure.

The ZFC M (T) of BF-0.20BT shows Curie-Weiss behaviour $\chi = C/(T-\theta_W)$ above $T_N$~608K, where C and $\theta_W$ are Curie constant and Curie-Weiss temperature, respectively. Fig. 3.6(b) shows the temperature dependence of the inverse DC susceptibility ($\chi^{-1}$) whose linear behaviour at high temperatures (T > 700 K) clearly confirms to Curie-Weiss law with $\theta_W$ = -873.6 K. The large negative value of $\theta_W$ indicates strong antiferromagnetic interactions and a LRO AFM state below $T_N$~608K. The effective magnetic moment ($\mu_{eff}$) of $Fe^{3+}$ ion, calculated from the Curie constant C, comes out to be 4.98 $\mu_B$ which is nearly 80% of the magnetic moment of $Fe^{3+}$ ions in the high spin configuration (S = 5/2), as expected for BF-0.20BT due to 20% Ti substitution at the Fe site. AFM structure of BF-0.20BT was further confirmed by neutron powder diffraction (NPD) studies.

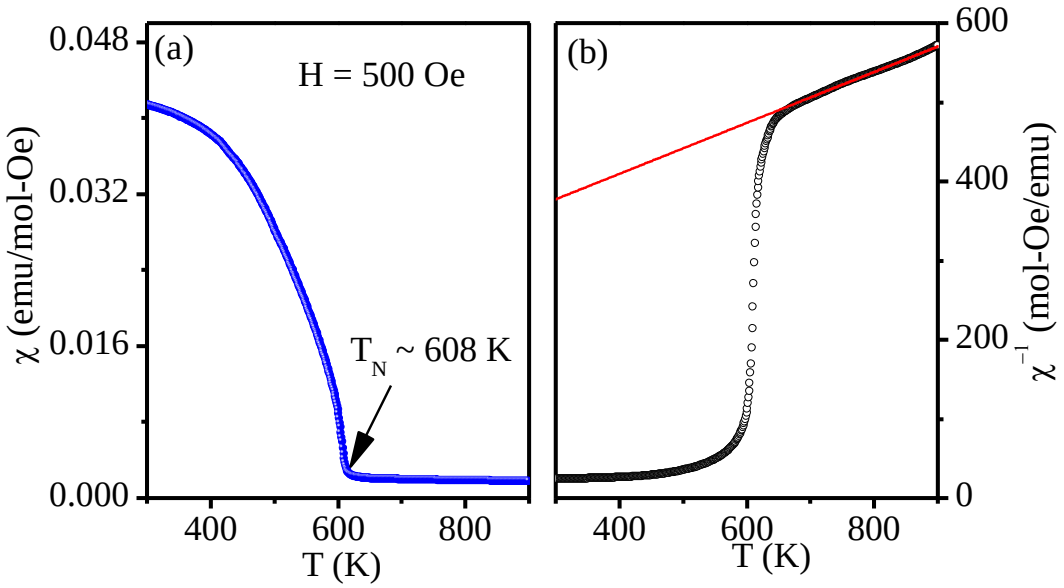


Figure 3.6: **(a)** ZFC DC magnetization versus temperature plot of BF-0.20BT for an applied field of 500 Oe **(b)** depicts the Curie-Weiss plot for BF-0.20BT above $T_N$**.**

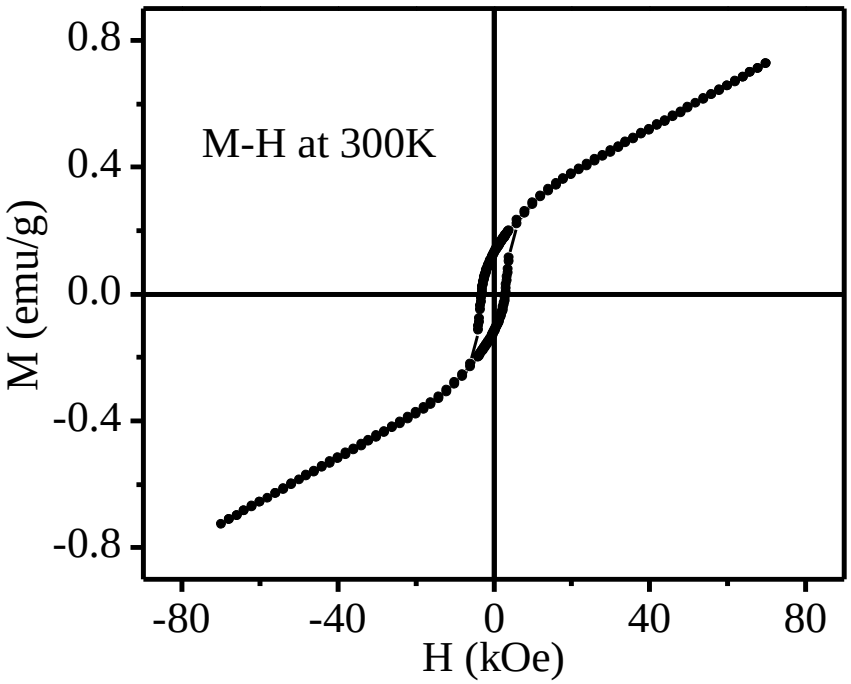


Figure 3.7: The M-H hysteresis loop at 300K for BF-0.20BT.

Fig. 3.8 shows the NPD pattern of BF-0.20BT at room temperature in the limited 2θ range of 15º -57º. This pattern contains main perovskite reflections as well as some superlattice reflections which arise either due to antiferromagnetic ordering or tilting of

oxygen octahedra. All the reflections could be indexed with respect to a doubled perovskite unit cell. The $111_{pc}$ (pc stands for pseudocubic unit cell) magnetic superlattice peak at $2\theta = 18.6^{o}$ (marked with an arrow) is not allowed in the rhombohedral R3c space group and arises due to AFM ordering of the Fe spins. Thus, the transition at $T_N$ ~608K in Fig. 3.6 (a) is linked with the appearance of a LRO AFM phase.

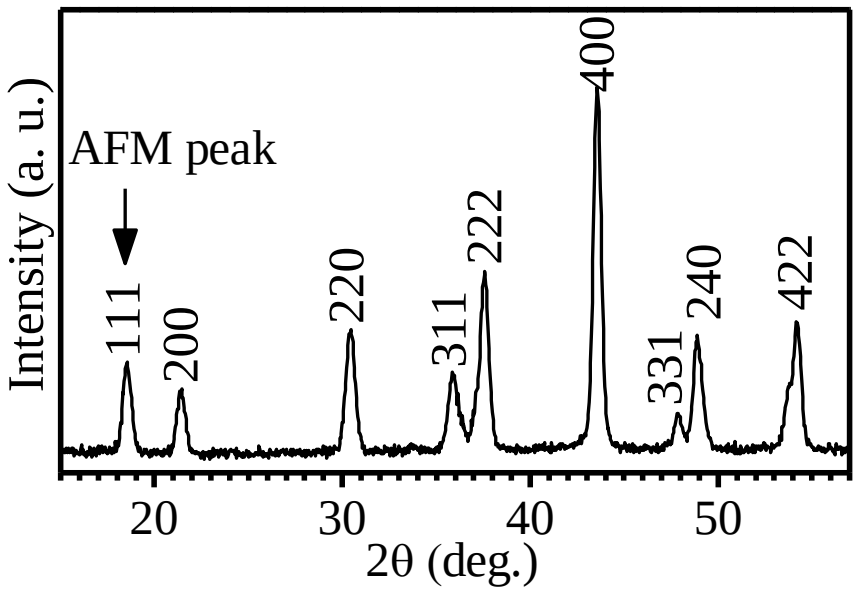


Figure 3.8: Neutron powder diffraction pattern of BF-0.20BT at room temperature. Arrow marks the antiferromagnetic peak. All the indices are written with respect to a doubled pseudocubic cell.

### 3.4.3.2 The low temperature magnetic transitions:

Below room temperature, the ZFC M(T) of BF-0.20BT clearly reveals three anomalies near 240K, 135K and 30K as can be seen from Fig. 3.9. In addition, the ZFC and FC M(T) curves show bifurcation due to history dependent effects. Such a bifurcation has been reported in spin glass and superparamagnetic (SPM) systems [24,41–43]. In canonical spin glasses, ZFC M(T) shows a cusp at $T_{max}$ and the bifurcation of FC and ZFC M(T) occurs close to the cusp temperature [41]. However, unlike the canonical systems, the peak around ~240 K in M(T) of BF-0.20BT is quite smeared out and the

bifurcation starts well above $T_{max}$. While smeared peaks have been reported in several cluster glass and SPM systems due to occurrence of freezing/blocking over a wide range of temperatures as a result of large distribution of cluster sizes [255–257], the peak around 240K is much more broad and the bifurcation of ZFC and FC M (T) curves occurs well above the peak temperature ($T_{max}$). The extent of broadening of the 240K peak in the ZFC M(T) measurements is dependent on the field strength as discussed in a later section. As shown in next section, the AC susceptibility peak is rather relatively sharper (see inset of Fig. 3.10(b)) than the peak in the ZFC M(T) for the 240K transition. Obviously, the time scales associated with different measuring probes give different widths for the 240K transition as expected for a glassy phase in a concentrated system with larger distribution of cluster sizes. What is significant is that the two different measurement probes, i.e. M(T) and AC susceptibility, clearly confirm that a transition is indeed taking place around 240K.

Below the 240K transition, the ZFC M(T) plot shows a kink around 135 K followed by a nearly temperature independent plateau upto ~30K. On further cooling below 30K, ZFC M(T) starts decreasing. The FC M(T) also shows a kink around 135K but below this temperature it keeps on increasing without any anomalous decrease around 30K. In polycrystalline $BiFeO_3$ sample [103] and single crystals of $BiFeO_3$ [102], two transitions around 260K and 30K, respectively, have been observed as discussed in previous chapter. Further, the transition around 140K has been investigated in great detail in $BiFeO_3$ and has been linked with electromagnons [111,114,116]. The electromagnons are collective spin and lattice excitations that can be excited by electric field. The electromagnons have been reported using terahertz [258] and Raman [111,114,116] spectroscopy as well as inelastic neutron scattering studies [237]. The first experimental evidence of electromagnons was demonstrated in $RMnO_3$ (R = Tb, Gd) using terahertz

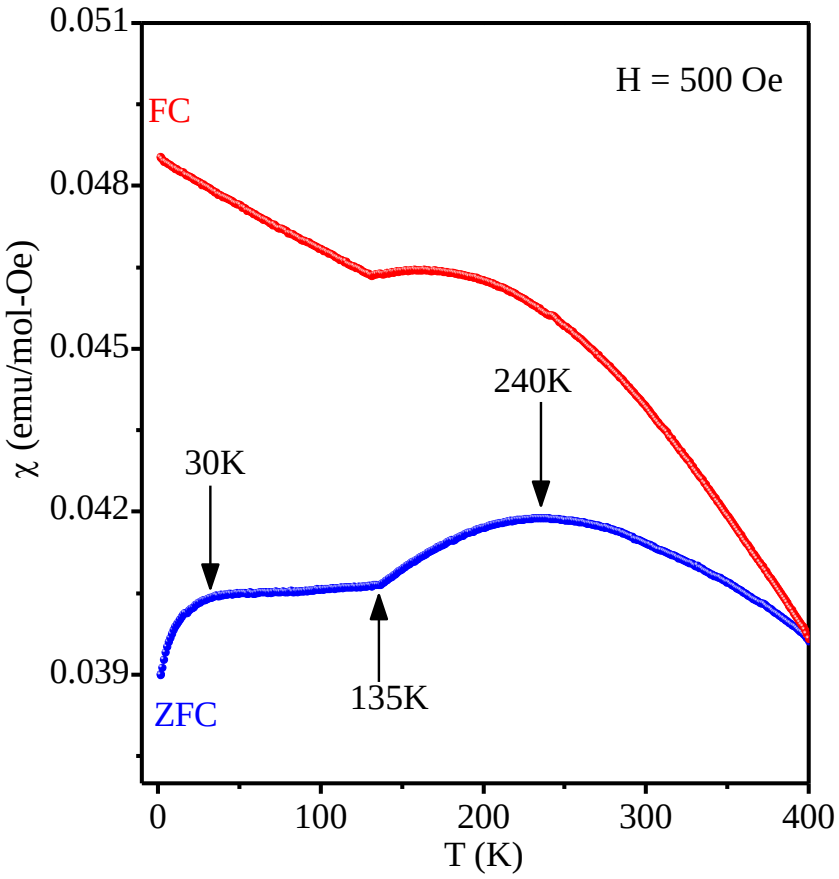


Figure 3.9: Temperature dependence of DC magnetization of BF-0.20BT under ZFC and FC conditions for an applied field of 500 Oe.

spectroscopy [258] whereas in $BiFeO_3$, the electromagnons were first reported using Raman spectroscopy [111,114,116] where the intensity and frequency of magnon modes appearing around 140K was shown to change on application of external electric field. The theoretical work of de Sousa and Moore [259] and Fishman et al. [260] have confirmed the existence of electromagnons in Raman scattering studies on $BiFeO_3$. In case of BF-0.20BT, the M(T) measurement reveals strong signature of 135K transition and shows an anomaly in the integrated intensity of the AFM peak in the neutron diffraction pattern (discussed later in section). We believe that this transition is also linked with electromagnons although, Raman scattering, THz spectroscopy and inelastic neutron

scattering studies are required to confirm this. As this is beyond the scope of the present work, we keep our focus on the other two transitions occurring around 240K and 30K in what follows hereafter.

### 3.4.4 Evidence for two spin-glass transitions in AC susceptibility of BF-0.20BT:

We carried out frequency dependent AC magnetic susceptibility ($\chi(\omega, T)$) measurements to understand whether the bifurcation of the ZFC and FC M(T) is associated with spin-glass freezing or SPM blocking. Figs. 3.10 (a) and (b) depict real ($\chi'(\omega, T)$) and imaginary ($\chi''(\omega, T)$) parts, respectively, of $\chi(\omega, T)$ of BF-0.20BT measured at various frequencies for a drive field of 2 Oe in the temperature range 2-300K. The $\chi'(\omega, T)$ shows two peaks at $T_{f1}$ and $T_{f2}$ corresponding to the two anomalies around ~240 and ~30K revealed in ZFC M(T) plot as can be seen from the insets (i) and (ii) of Fig. 3.10(a). It is noteworthy that the temperature dependence of $\chi''(\omega, T)$ for the 240K anomaly exhibits normal freezing behavior whereas it shows anomalous behavior with negative cusp for the 30K anomaly. The negative cusp is in agreement with that reported in single crystals of $BiFeO_3$ as well as in polycrystalline samples of $BiFeO_3$ [102]. The anomalous frequency dependence of the lowest temperature SG phase (SG2) has been discussed in detail in the context of pure $BiFeO_3$ where the role of cycloidal magnetic structure has been highlighted [102]. However, the spin cycloid of $BiFeO_3$ is known to be destroyed in the presence of disorder, such as 20% $BaTiO_3$ substitution in the present case. This has been confirmed by neutron scattering and magnetization measurements [90,91]. Suffice is to say that the opening of the M-H loop in our samples (see Fig. 3.7) rules out the presence of spin cycloid and therefore there is no correlation between the anomalous frequency dispersion [see Ref. [102] for more details] of the 30K anomaly and the spin cycloid. We believe that this anomalous behaviour is linked with

the LCR circuit resonance frequency as pointed out in Ref. [102] and discussed in the previous chapter.

The peak corresponding to the 240K transition is relatively less broad in $\chi'$ ($\omega$, T) and $\chi''$ ($\omega$, T) as compared to that in the ZFC M(T) (see Fig. 3.9) indicating the role of time scales associated with the spin freezing/blocking process and the measurement time for different probes. The temperatures $T_{f1}$ and $T_{f2}$ corresponding to the two peaks in $\chi'$ ($\omega$, T) shift towards higher side on increasing the measuring frequency. Such a frequency dependent shift may be due to either SG freezing or SPM blocking [24,41–43]. The shift of the $\chi'$ ($\omega$, T) peak temperature has been analyzed in terms of an empirical frequency sensitivity parameter $K = \Delta T_f / (T_f \Delta(\ln \omega)$, the so-called Mydosh parameter [42], which lies in the range 0.003-0.08 [42] and 0.1 to 0.3 [42] for spin-glass freezing and SPM blocking, respectively. In the case of BF-0.20BT, $K$ is found to be ~0.04 for both the transitions which supports the spin-glass freezing rather than SPM blocking.

For SPM blocking, the relaxation time ($\tau$) should follow the typical Arrhenius type dependence without any critical slowing down behaviour [198]:

$$\tau = \tau_0 \exp(E_a / k_B T), \qquad \ldots\ldots (3.1)$$

where $\tau$ is the relaxation time, $E_a$ the activation energy, $k_B$ the Boltzmann constant, and $\tau_0$ the inverse of the attempt frequency. The ln ($\tau$) vs 1/T plots derived from the frequency dependent peak positions $T_f(\omega)$ of $\chi'$ ($\omega$, T) for the transitions around 240 K and 30 K are therefore expected to be linear for SPM blocking. The fact that this plot is non-linear in BF-0.20BT, as can be seen from Figs. 3.11(a) and (b)), rules out the SPM blocking being responsible for the two peaks in $\chi'$ ($\omega$, T). For spin glass freezing, one observes critical slowing down of the relaxation time ($\tau$) due to ergodicity breaking. This has been modelled using a power law [261]:

$$\tau = \tau_0 [(T_f - T_{SG})/T_{SG}]^{-z\nu}, \qquad \ldots\ldots\ldots (3.2)$$

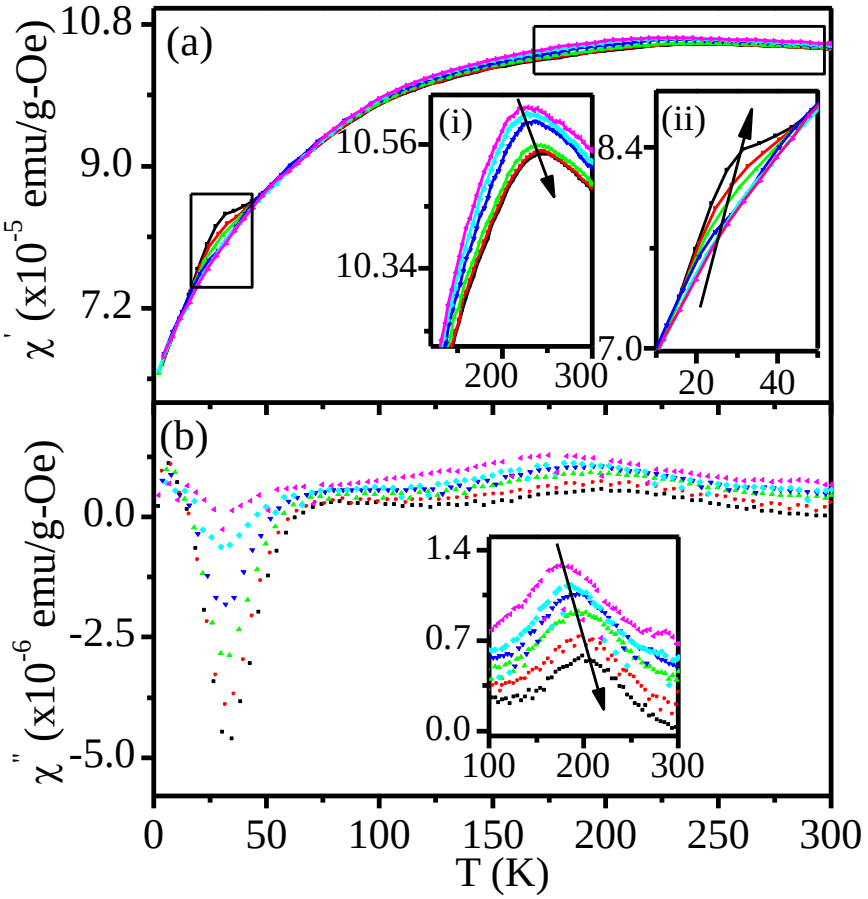


Figure 3.10: Variation of χ' (ω, T) and χ'' (ω, T) in the temperature range 2-300K at various frequencies [47.3 Hz (►), 97.3 Hz (◄), 197.3 Hz (▼), 297.3 Hz (▲), 397.3 Hz (●), 497.3 Hz (■)]. Insets (i) and (ii) depict χ' (ω, T) on a zoomed scale for SG 1 and SG 2, respectively.

where, $T_{SG}$ is the SG transition temperature, ν the critical exponent for the correlation length (ξ) and z the dynamical exponent relating τ to ξ. In some spin glass systems [224], the frequency dependent shift of the χ' (ω, T) peak temperature has been modelled using the empirical Vogel–Fulcher (V-F) law also [224]:

$$\tau = \tau_0 \exp(E_a / k_B (T_f - T_{SG}), \qquad \ldots\ldots(3.3)$$

where $E_a$ is the activation energy. Both the power law and V-F law type critical dynamics provide excellent fits for the two transitions, as can be seen from Figs. 3.11 and 3.12, respectively. The continuous line in Figs. 3.11(a) and (b) are the fits for the V-F law. Both the fits are excellent. The least squires fitting parameters for the two transitions are:

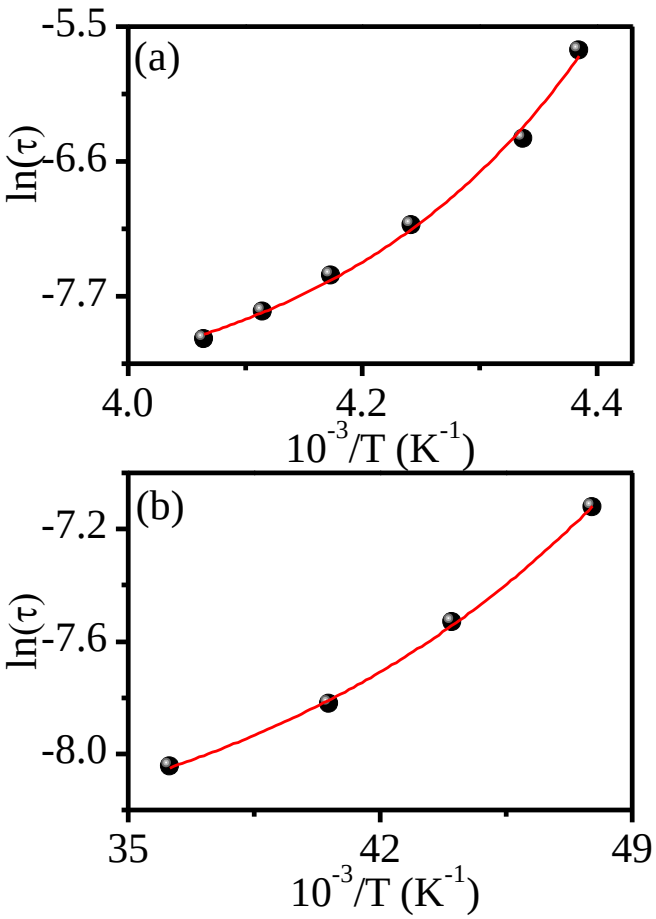


Figure 3.11: ln(τ) versus 1/T plot for (a) SG1 and (b) SG 2 transitions. Solid line is the least squares fit for Vogel-Fulcher law.

$T_{SG1}$~ (218.6±0.8) K, $z\nu_1$ = 2.09 s, $\tau_{01}$ = 3.87x10$^{-6}$ s and $T_{SG2}$ = (18.6±0.4) K, $z\nu_2$ = 0.69, and $\tau_{02}$ = 1.92x10$^{-4}$s for power law and $T_{SG1}$ ~(214±2) K, $E_{a1}$ = 4.89 meV, and $\tau_{01}$ = 5.64x10$^{-6}$s and $T_{SG2}$ ~(15.9±0.1) K, $E_{a2}$ = 0.65 meV, and $\tau_{02}$ =1.64x10$^{-4}$ s for V-F law. The values of $T_{SG1}$ and $T_{SG2}$ as well as $\tau_{01}$ and $\tau_{02}$ obtained by V-F law and power law type critical dynamics are comparable. Thus, both the power law and V-F dynamics confirm the glassy nature of the two frequency dependent anomalies in $\chi'(\omega, T)$. The magnitude of $\tau_{01}$ and $\tau_{02}$ for both the power law and V-F law type dynamics falls in the typical cluster glass (CG) category (10$^{-5}$-10$^{-10}$s) for concentrated systems [24] [42] and not the

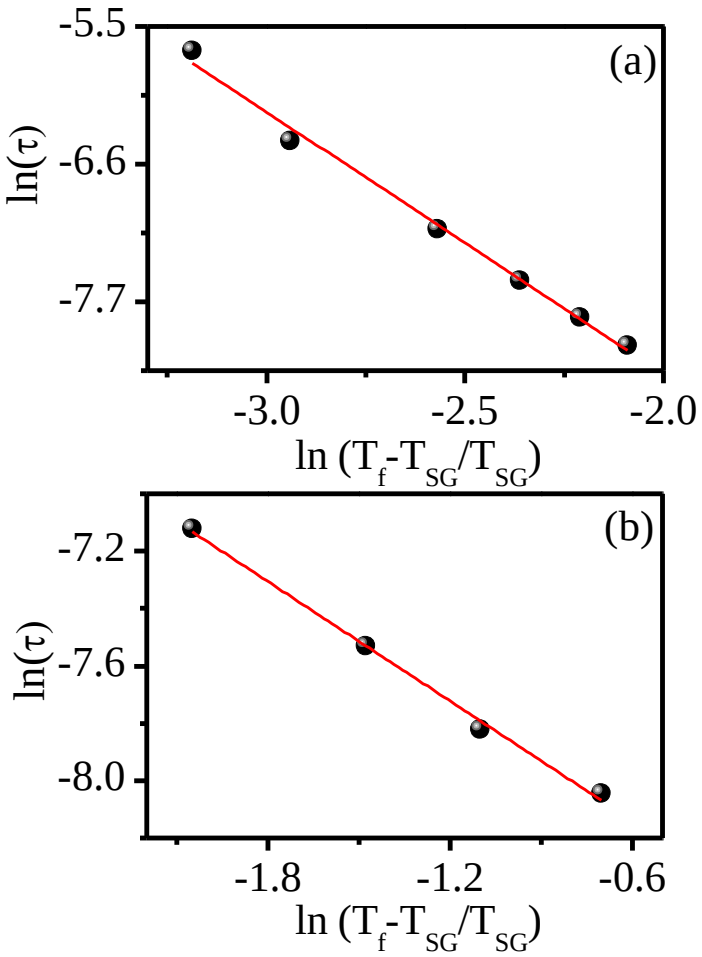


Figure 3.12: ln(τ) versus ln(T-$T_{SG}$/$T_{SG}$) plot for (a) SG1 and (b) SG2 transitions. Solid line shows the least squares fit for power law.

canonical spin glasses in dilute systems [24,42] which is much smaller due to involvement of atomic spins in the glassy freezing.

### 3.4.5 Evidence for de Almeida-Thouless and Gabay-Toulouse lines in BF-0.20BT:

The existence of two spin-glass phases, which we shall label as SG1 and SG2 hereafter, was further confirmed by the presence of the so-called de Almeida-Thouless (A-T) [49] and Gabay-Toulouse (G-T) [50–53] lines. For Ising systems, it has been shown by de Almeida and Thouless [49] that the peak temperature ($T_{max}$) of the ZFC M (T) plot shifts to lower temperature side on increasing the magnetic field (H) as a result of

replica symmetry breaking [49]. For low fields, this shift shows the following H dependence:

$$H^2 = A[1- T_{max}(H)/T_{max}(0)]^3, \qquad \ldots\ldots(3.4)$$

where $T_{max}(H)$ and $T_{max}(0)$ are the field dependent and zero-field freezing temperatures, respectively. Eq. (3.4) sets the boundary between ergodic paramagnetic and non-ergodic spin-glass phases and is commonly known as the A-T line [49]. For the Heisenberg systems also, it has been shown that the A-T line is present and $T_{max}$ follows $H^{2/3}$ dependence at low fields [50–53]. However, it can occur due to freezing of either the longitudinal ($q_{ll}$) or the transverse ($q_{\perp}$) components of the spin, depending on whether the single ion anisotropy (D/J) is positive or negative. For low values of D/J, a second SG transition whose $T_{max}$ decreases as $H^2$ at low fields is predicted to occur due to the freezing of the second component of the spin. For small but positive values of D/J, as is the case with $BiFeO_3$ [237], the first SG transition (i.e. SG1) is expected to be due to the freezing of $q_{ll}$ component while the second one (i.e. SG2) due to freezing of $q_{\perp}$ as per the theoretical predictions [50–53]. The H dependence of the $q_{ll}$ and $q_{\perp}$ freezing temperatures should thus fix the A-T and G-T lines in the $T_{max}$ versus H phase diagram for the SG1 and SG2 phases, respectively.

To verify the existence of A-T and G-T lines in BF-0.20BT, we carried out ZFC M (T) measurements at different fields and the results are depicted in Fig. 3.13 for both the transitions. It is evident from the figure that the peak corresponding to SG1 transition is prominent, even though broad, while no such peak, except a step, is observed for SG2 transition up to a field of 500 Oe. With increasing field, the peak corresponding to SG2 transition also starts taking a prominent shape (see insets), while the peak corresponding to the SG1 transition starts getting smeared out and suppressed after initial sharpening

upto 800 Oe. We find that the $T_{max}$ for both the transitions decreases with increasing magnetic field as expected theoretically. The linear nature of the $T_{max}$ versus $H^{2/3}$ and $T_{max}$

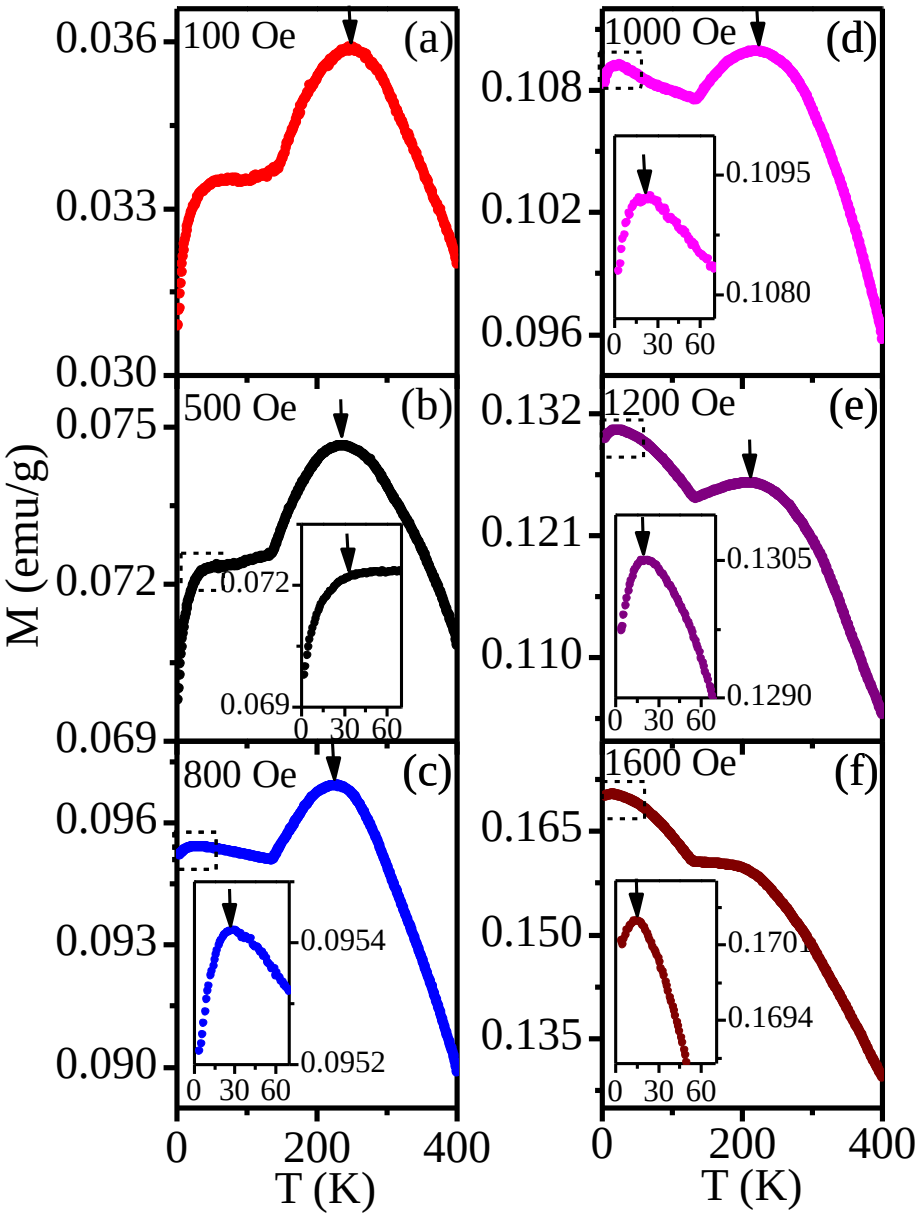


Figure 3.13: ZFC DC magnetization vs temperature plots of BF-0.20BT measured at different applied fields. Insets depict the magnified view around SG2 transition.

vs $H^2$ plots shown in Figs. 3.14(a) and 3.14(b) for the SG1 and SG2 transitions confirms the existence of A-T and G-T lines, respectively, in the $T_{max}$ versus H phase diagram. Thus our results confirm the theoretical predictions [50–53] for two spin-glass transitions in Heisenberg systems with low D/J.

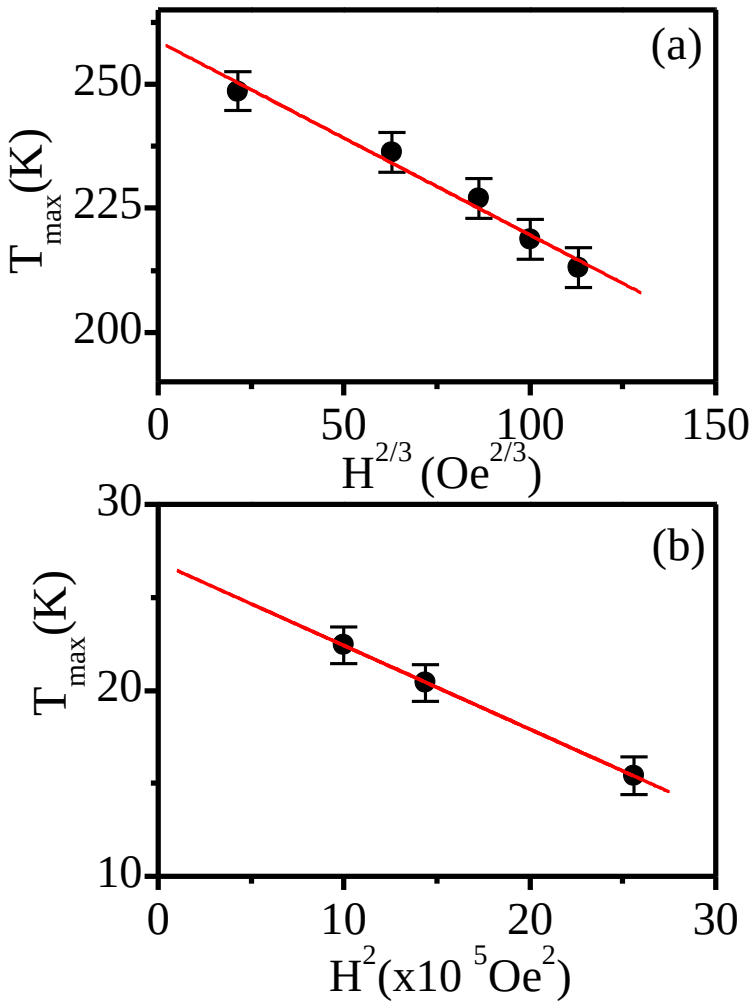


Figure 3.14: (a) de Almeida-Thouless (A-T) line for SG1 transition and (b) Gabay-Toulouse (G-T) line for SG2 transition.

### 3.4.6 Relaxation of thermoremanent magnetization for the spin glass phases of BF-0.20BT:

Spin glass state is known to exhibit slow relaxation of thermoremanent magnetization which has been modelled using stretched exponential function [262,263]:

$$M(t) = M_0 + M_r \exp[-(t/\tau)^{1-n}] \qquad \text{…….(3.5)}$$

where $M_0$ is the intrinsic ferromagnetic component, $M_r$ the glassy component, $\tau$ the characteristic relaxation time and n the stretched exponential exponent. To study the slow

relaxation of the thermoremanent magnetization, we cooled the sample under a field of 1T from 300 K to 200K for the SG1 phase. After reaching the set temperatures, the sample was allowed to age without switching off the field for a waiting time of $t_w$ = 500s. After a waiting time of $t_w$=500s, the field was switched off. For the SG2 phase, the sample was first annealed at 773 K above $T_N$ to remove any remanent magnetization introduced during the first cycle and then cooled to 10K under 1T field. This was followed by the protocol identical to that adopted for the SG1 phase. The thermoremanent magnetizations so measured as a function of time are shown in Figs. 3.15(a) and (b) at

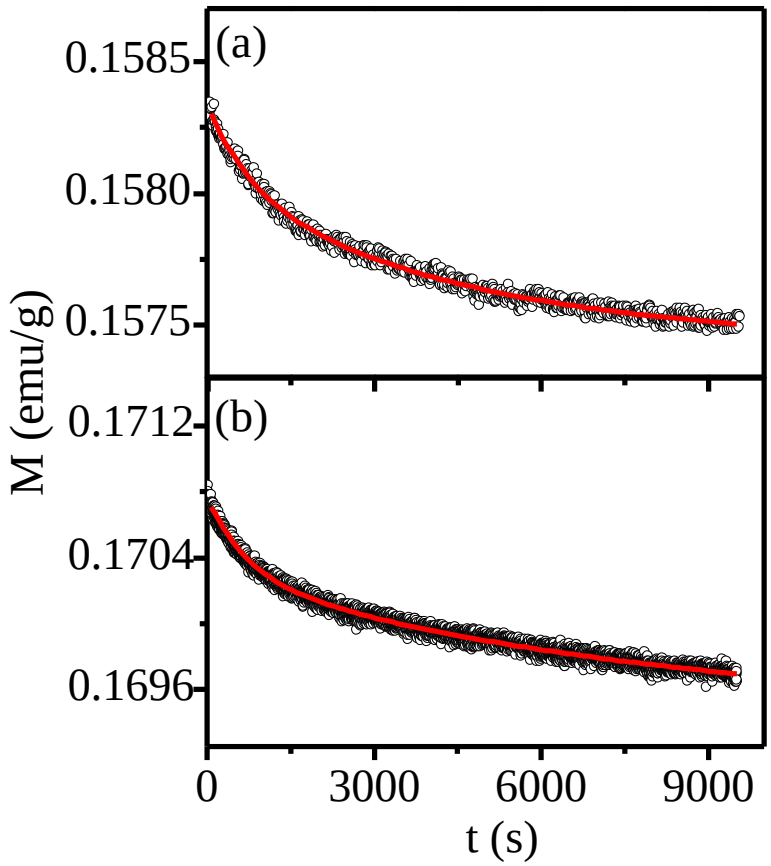


Figure 3.15: Variation of thermoremanent remnant magnetization (M (t)) with time at (a) 200 K and (b)10 K for BF-0.20BT.

200K and 10K, respectively. The continuous line in the two figures depicts the best fit for Eq. (5). These fits yield n, $M_0$, $M_r$ and $\tau$ as 0.55, 0.1575 emu/g, 0.0008 emu/g, (1207±15)s for the SG1 phase and 0.53, 0.1697 emu/g, 0.0009 emu/g, (1661±14)s for the SG2 phase, respectively. The observed exponent (n) and relaxation time ($\tau$) are in agreement with the reported values for cluster glasses and super spin glasses [263]. Thus, relaxation behaviour of thermoremanent magnetization also favours the existence of two SG phases in BF-0.20BT.

### 3.4.7 Evidence for magnetoelastic coupling at spin-glass transitions in BF-0.20BT:

In order to verify if the two SG transitions and the intervening transition driven by electromagnons involve any structural phase transition, we carried out XRD studies in the temperature range 12K to 350K. Fig. 3.16 depicts the temperature evolution of the XRD profiles of a few selected pseudocubic (pc) peaks ($222_{pc}$, $400_{pc}$ and $440_{pc}$ reflections) of BF-0.20BT after stripping off the $K_{\alpha 2}$ contribution. It is evident from this figure that the $222_{pc}$ and $440_{pc}$ peaks are doublets, whereas $400_{pc}$ is a singlet, as expected for the rhombohedral structure, down to 12K which implies absence of any structural phase transition below room temperature. This was further confirmed by Rietveld refinements at different temperatures. The excellent fits confirm the R3c space group for BF-0.20BT at all temperatures. Fig. 3.17 depicts the observed, calculated and difference profiles obtained after the Rietveld analysis of the XRD patterns at selected temperatures 300K, 200K, 100K and 12K, respectively, for BF-0.20BT using R3c space group. Thus, our Rietveld refinements also confirm that there is no structural phase transition down to 12K. While the magnetic measurements clearly indicate the existence of SG1 and SG2 transitions in BF-0.20BT, the reason for the broad nature of the peak in the ZFC M(T) of the SG1 transition needs to be understood. In order to rule out the role of a structural phase transition, which might have been missed in the medium resolution rotating anode

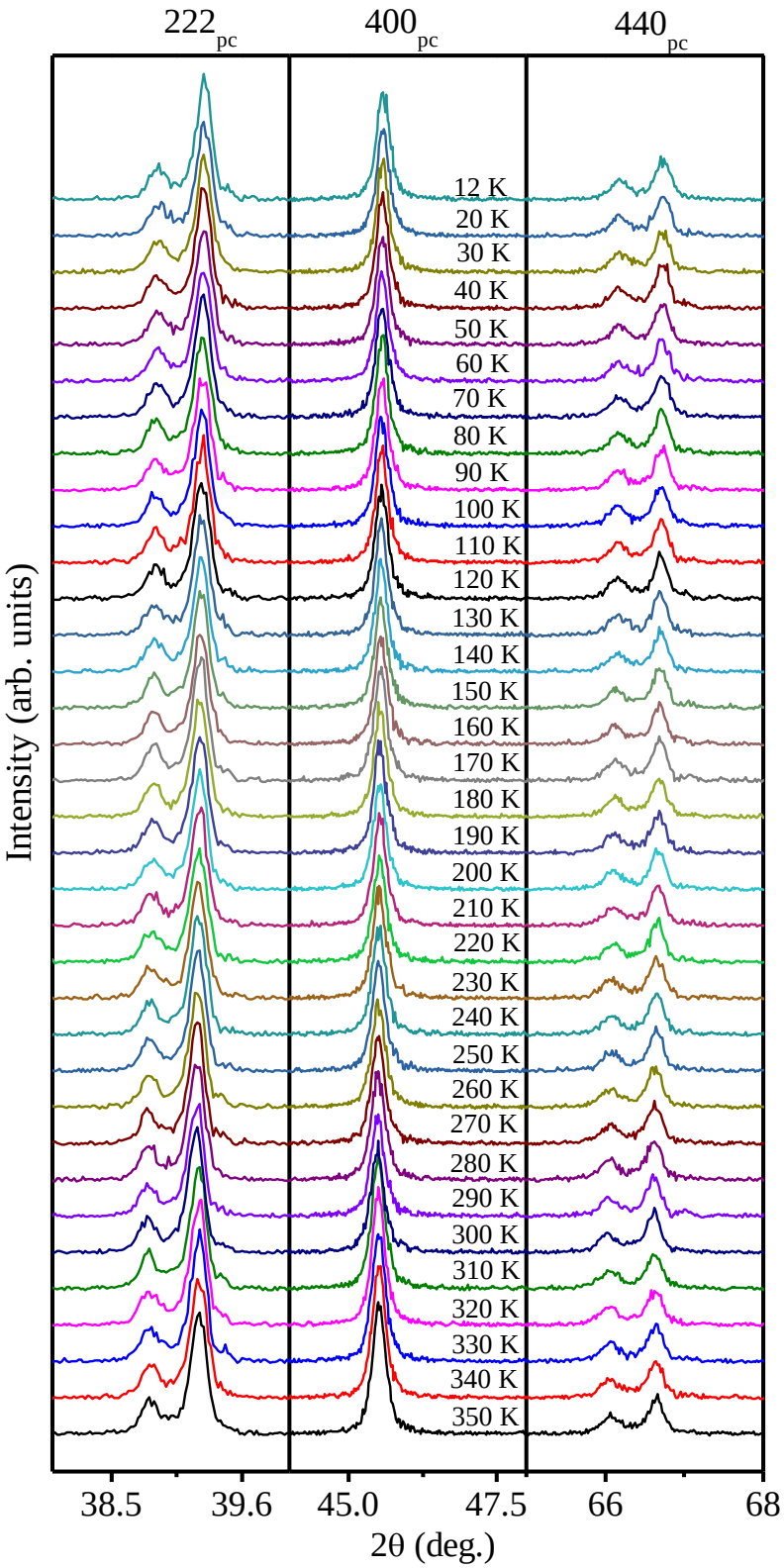


Figure 3.16: The evolution of x-ray powder diffraction profiles of the $(222)_{pc}$, $(400)_{pc}$ and $(440)_{pc}$ reflections of BF-0.20BT with temperature showing absence of any structural phase transition.

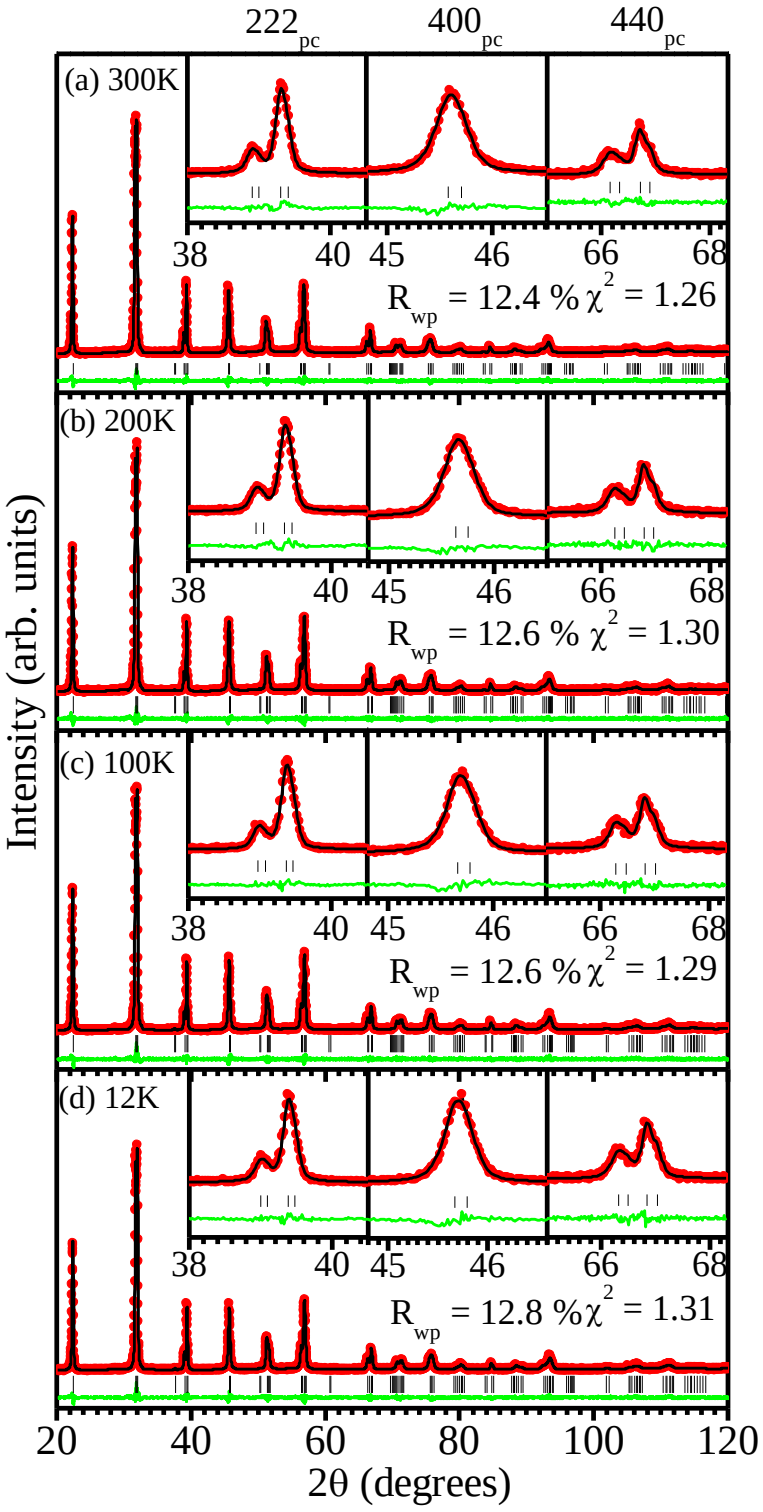


Figure 3.17: Observed (filled circles), calculated (continuous line), and difference (bottom line) profiles obtained from Rietveld refinement using R3c space group at (a) 300K (b) 200K (c)100K and (d) 12K. The vertical tick marks correspond to the position of all allowed Bragg reflections.

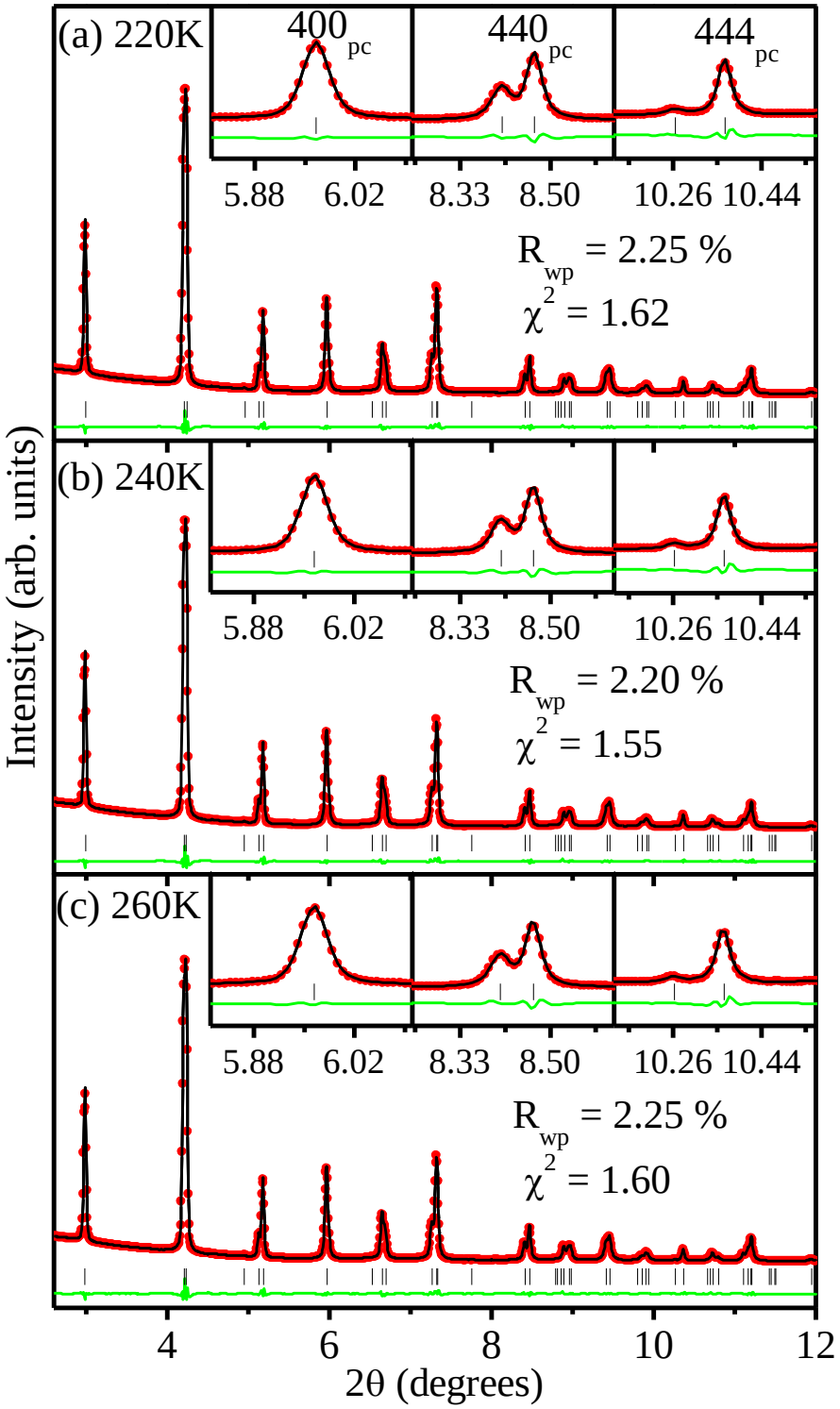


Figure 3.18: Observed (filled circles), calculated (continuous line), and difference (bottom line) profiles obtained from the Rietveld refinement using SXRD data at (a) 220K (b) 240K and (c) 260K using R3c space group for BF-0.20BT. The vertical tick marks above the difference profile represents the Bragg peak positions.

based XRD data, we also carried out Rietveld refinement using high resolution synchrotron x-ray diffraction (SXRD) patterns at three selected temperatures 260K, 240K and 220K. Fig. 3.18 depicts the observed, calculated and difference profiles obtained after the Rietveld analysis of the SXRD patterns at 260K, 240K and 220K, respectively, for BF-0.20BT using R3c space group. The excellent fit between observed and calculated profiles confirms that the R3c space group for BF-0.20BT at room temperature does not change across the SG1 transition. We can thus conclusively rule out the role of any structural phase in the broad SG1 transition.

Even though there is no structural phase transition, the temperature dependence of unit cell volume ($V_{hex}$), as obtained from the Rietveld refinements, shows anomalies around the three magnetic transitions (see Fig. 3.19). It is interesting to note that the slope of the experimental $V_{hex}$ versus T plot changes prominently around the SG1 transition without any discontinuous change in the value of $V_{hex}$. After the initial change of slope, the experimental $V_{hex}$ values decrease smoothly with temperature below SG1 transition upto~150K. Small changes in volume around 140K and SG2 transitions are also observed as shown in the inset of Fig. 3.19.

The large change of slope around the SG1 transition suggests strong magnetoelastic coupling associated with this transition. It is possible to separate out the magnetic (magnetoelastic) contribution from the anharmonic lattice part at least for the SG1 transition because of the large slope change. For this, the temperature dependence of $V_{hex}$ above $T_{SG1}$ was modeled using the Debye-Grüneisen equation [264]:

$$V \cong V(0) + \frac{9\gamma N k_B}{B} T \left( \frac{T}{\Theta_D} \right)^3 \int_0^{\Theta_D/T} \frac{x^3}{e^x - 1} dx \quad \ldots\ldots\ldots (3.6),$$

where V(0), $\Theta_D$, $\gamma$ and B are the unit cell volume at 0K, the Debye temperature, the Grüneisen parameter and the bulk modulus, respectively. Continuous solid line in the figure shows the results of least squares fit to the observed unit cell volume in the temperature range 260K <T≤ 350K using Eq. (3.6). The fitting parameters so obtained are: V (0) = (375.86 ± 0.01) Å$^3$, $\Theta_D$ = (594 ± 10) K, and $9\gamma Nk_B/B$ = (0.071 ± 0.003) Å$^3$/K. The difference $\Delta V$ between the experimentally observed values of $V_{hex}$ and the theoretically calculated anharmonic lattice contribution increases with decreasing temperature. It is interesting to note that the bulk strain ($\Delta V/V$) vs $M_s^2$ plot corresponding to the shaded region in the figure is linear in the temperature range 240 to 150K as can be seen from Fig. 3.20. This linear dependence confirms that the slope change is due to

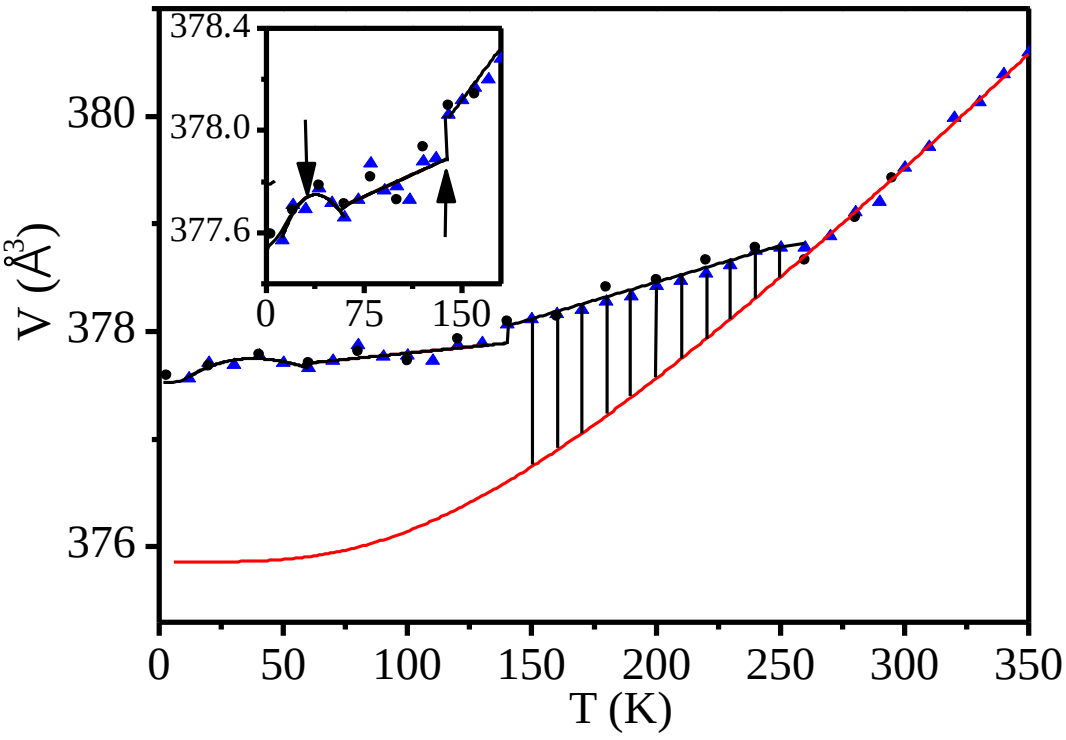


Figure 3.19: Variation of unit cell volume with temperature: XRD (▲) and NPD (●) data. Solid line (—) is fit for Debye Grüneisen equation $T_{SG1}$. Inset shows the zoomed view around 140K and SG2 transitions.

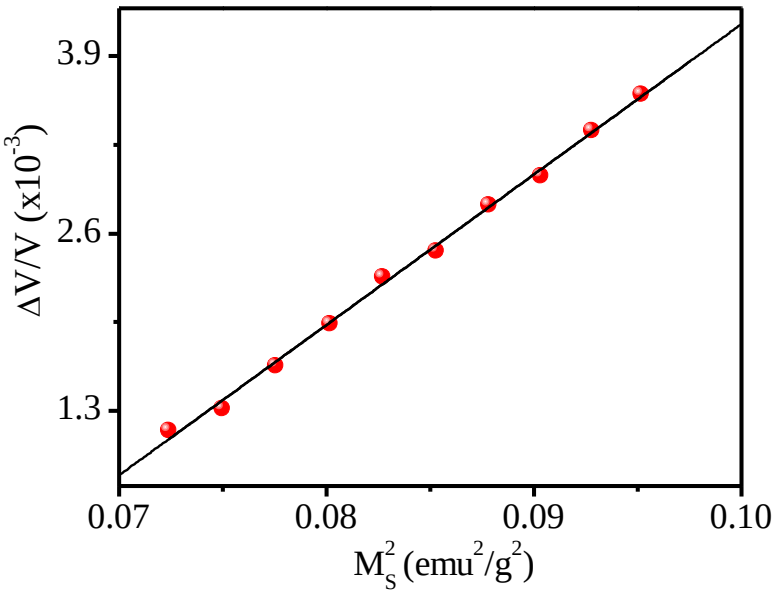


Figure 3.20: Variation of volume strain (ΔV/V) against square of magnetization ($M_S^2$) obtained by M-H loop.

quadratic spin-lattice coupling [264]. The fact that the change of slope is much more pronounced around SG1 as compared to that around 140 and SG2 transitions suggests that the spin-lattice coupling for the other two transitions is rather weak as compared to that for the SG1 phase.

### 3.4.8 Evidence for coexistence of LRO AFM and spin-glass phases in BF-0.20BT:

We now turn towards neutron diffraction studies to understand whether the LRO, SG1 and SG2 transitions occur on the same magnetic sublattice or not. Fig. 3.21 depicts the temperature evolution of the neutron powder diffraction patterns of BF-0.20BT in the limited 2θ range of 15-57º. It was verified by Rietveld refinement that neither the nuclear nor the magnetic structure changes down to the lowest temperature of measurement. The asymmetric unit of rhombohedral structure with R3c space group is already given in section 3.4.2. All the nuclear structure peaks are well indexed with respect to the nuclear unit cell of the R3c space group except the magnetic peaks. No evidence for any magnetic impurity phase was found in the neutron data. The magnetic peaks are indexed by

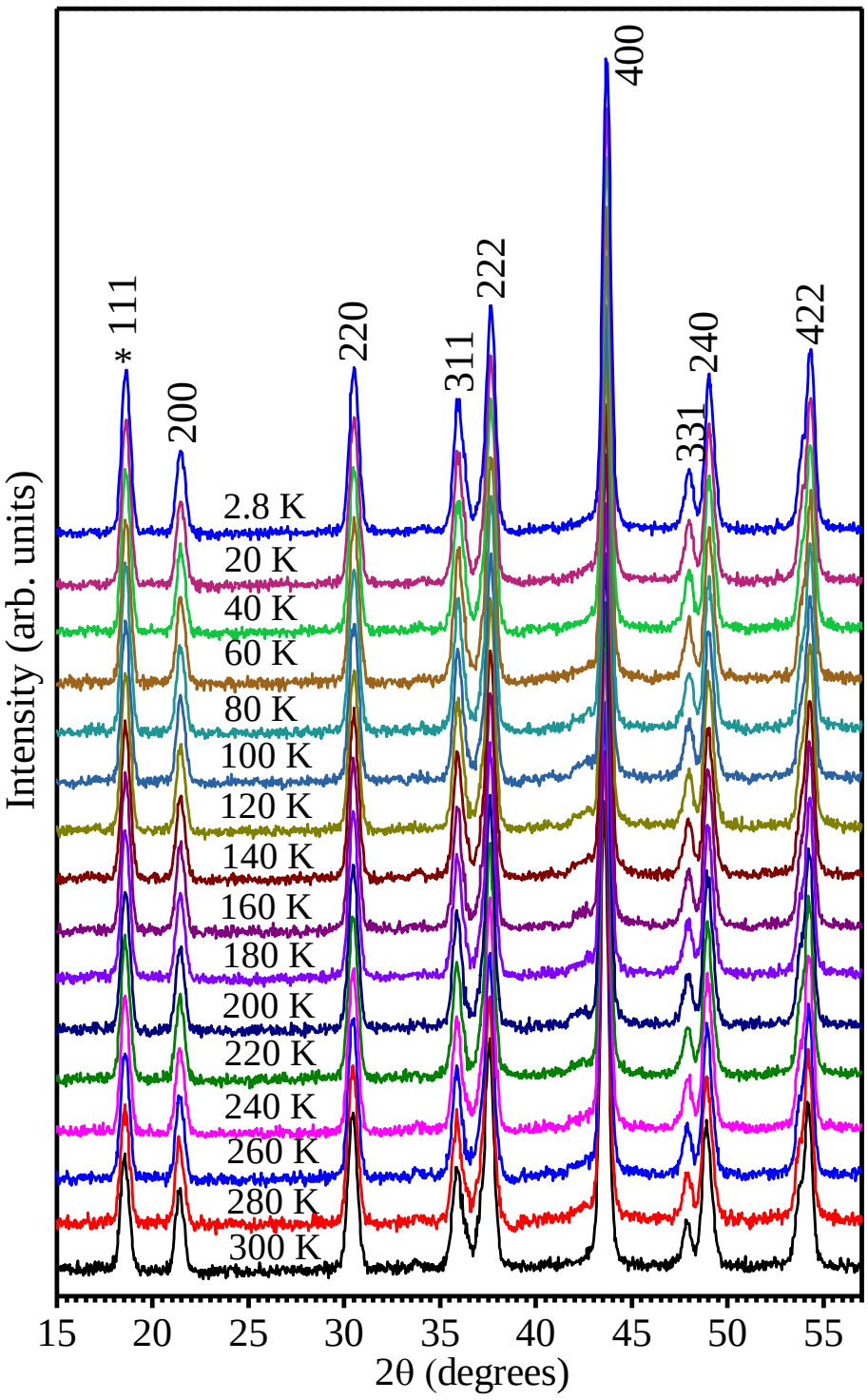


Figure 3.21: The evolution of the neutron powder diffraction patterns with temperature in the limited 2θ = 15º-57º range. The first peak is due to AFM ordering. The Miller indices are written with respect to a doubled pseudocubic cell.

considering additional phase in the nuclear structure refinement of neutron powder diffraction (NPD) data. We use the representation analysis to determine the magnetic structure of BF-0.20BT. For propagation vector k = (0,0,0), the little group $G_k$ formed by those elements of space group that leave k invariant or only changed by a translation of the reciprocal lattice coincide with the space group R3c. The irreducible representations corresponding to propagation vector k = (0,0,0) are given in Table 3.3. In hexagonal unit cell with R3c space group, the magnetic ions $Fe^{3+}$ occupy the 6(a) Wyckoff site with general positions (0, 0, z) and (0, 0, z+1/2). The magnetic reducible representation $\Gamma_{mag}$ for the 6(a) Wyckoff site can be decomposed as direct sum of three irreducible representations,

$$\Gamma\ (6a/\ Fe) = 1\Gamma_1^1 + 1\Gamma_2^1 + 2\Gamma_3^2 \qquad \text{.....(3.7)}$$

The basis vectors associated with each irreducible representation are given in Table 3.4. The $\Gamma_1$ and $\Gamma_2$ representations are one dimensional whereas the representation $\Gamma_3$ is two dimensional. $\Gamma_1$ and $\Gamma_2$ correspond to single basis vector magnetic structures while $\Gamma_3$ corresponds to four basis vector magnetic structure. Following Singh et al. [90], the magnetic structure of BF-0.20BT corresponds to the representations $\Gamma_1$ and $\Gamma_3$ since the magnetic structure corresponding to the representation $\Gamma_2$ fails to model the magnetic reflections. The representations $\Gamma_1$ and $\Gamma_3$ gives similar values for structural as well as magnetic parameters within the standard deviation. Following Singh et al. [90], we use the $\Gamma_1$ representation for the magnetic structure analysis of BF-0.20BT. All the magnetic peaks were well indexed with propagation vector $\vec{k} =$ (0,0,0) and $\Gamma_1$ representation. The initial input parameters for Rietveld refinement of nuclear structure were taken from the Rietveld refinement using SXRD data. Both the nuclear and magnetic structures were refined, and the refinement converged successfully after a few

cycles. The observed (filled-circles) and calculated (continuous line) profiles show excellent fits at all temperatures and some selected fits obtained after Rietveld refinement at 300 K, 200K, 100K and 2.8K are shown in Fig. 3.22 (a) (b) (c) and (d), respectively. The refined lattice parameters, positional coordinates, thermal parameters, and magnetic

**Table 3.3.** Irreducible representation of the little group $G_k$ for propagation vector is k = (0,0,0).

| Irreps | Symmetry operators of $G_k$ | | | | | |
|---|---|---|---|---|---|---|
| | 1 | 3+ 0,0,z | 3- 0,0,z | c x,-x,z | c x,2x,z | c 2x,x,2z |
| $\Gamma_1$ | 1 | 1 | 1 | 1 | 1 | 1 |
| $\Gamma_2$ | 1 | 1 | 1 | -1 | -1 | -1 |
| $\Gamma_3$ | $\begin{pmatrix}1 & 0\\0 & 1\end{pmatrix}$ | $\begin{pmatrix}a & 0\\0 & b\end{pmatrix}$ | $\begin{pmatrix}b & 0\\0 & a\end{pmatrix}$ | $\begin{pmatrix}0 & 1\\1 & 0\end{pmatrix}$ | $\begin{pmatrix}0 & b\\a & 0\end{pmatrix}$ | $\begin{pmatrix}0 & a\\b & 0\end{pmatrix}$ |

**Table 3.4:** The basis vectors of the irreducible representations of the space group R3c appearing in the magnetic representation at the Wyckoff position 6a for the wave vector k = (0, 0, 0).

| Irreps | Basis vector | Atom 1 (0, 0, z) | | | Atom 2 (0, 0, z+½) | | |
|---|---|---|---|---|---|---|---|
| | | $m_x$ | $m_y$ | $m_z$ | $m_x$ | $m_y$ | $m_z$ |
| $\Gamma_1$ | $\psi_1$ | 0 | 0 | 3 | 0 | 0 | -3 |
| $\Gamma_2$ | $\psi_2$ | 0 | 0 | 3 | 0 | 0 | 3 |
| $\Gamma_3$ | $\psi_3$ | $\frac{3}{2}-i\frac{\sqrt{3}}{2}$ | $-i\sqrt{3}$ | 0 | 0 | 0 | 0 |
| | $\psi_4$ | 0 | 0 | 0 | $-\frac{3}{2}-i\frac{\sqrt{3}}{2}$ | $-\frac{3}{2}+i\frac{\sqrt{3}}{2}$ | 0 |
| | $\psi_5$ | 0 | 0 | 0 | $-\frac{3}{2}+i\frac{\sqrt{3}}{2}$ | $-\frac{3}{2}-i\frac{\sqrt{3}}{2}$ | 0 |
| | $\psi_6$ | $\frac{3}{2}+i\frac{\sqrt{3}}{2}$ | $i\sqrt{3}$ | 0 | 0 | 0 | 0 |

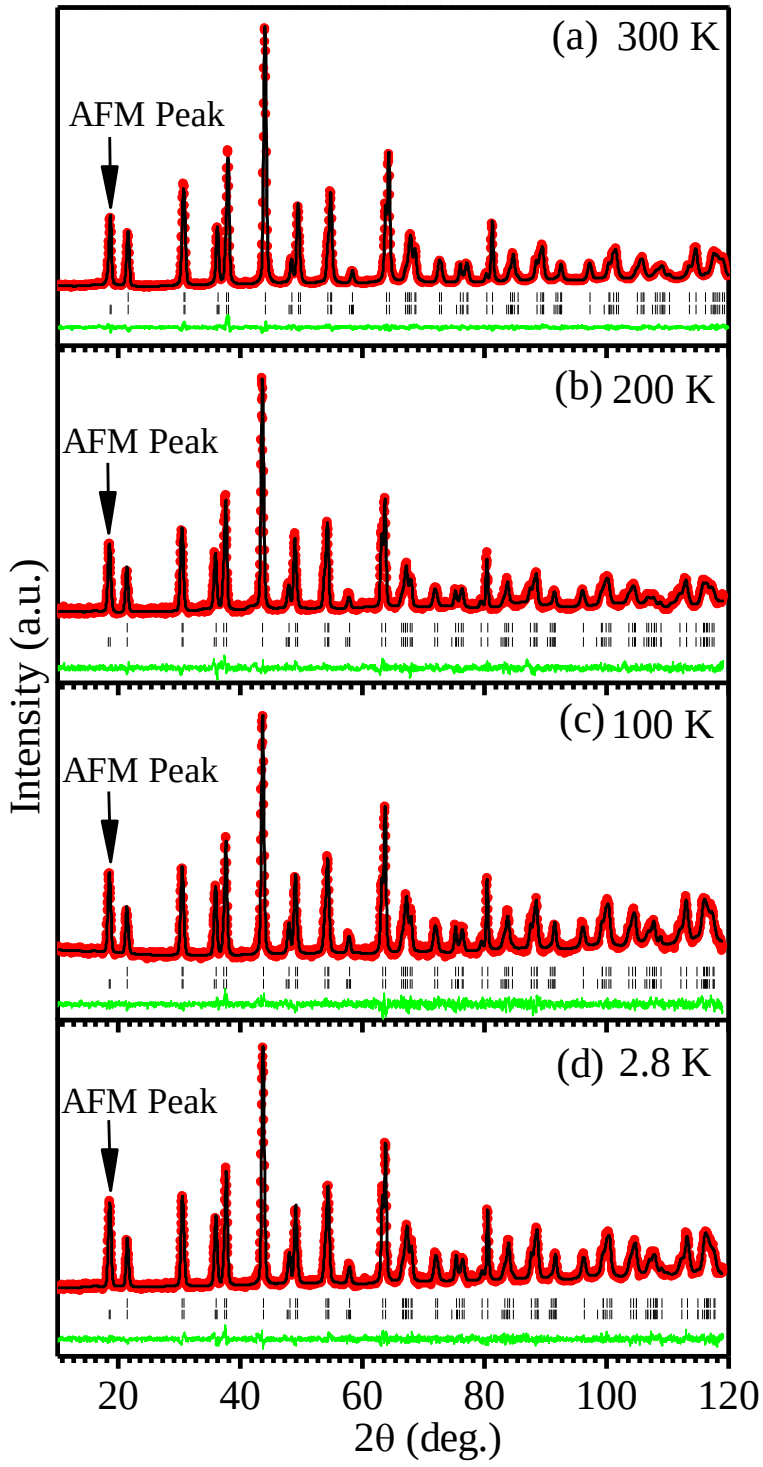


Figure 3.22: Observed (filled circles), calculated (continuous line), and difference (bottom line) profiles obtained from Rietveld refinement using R3c space group at (a) 300K (b) 200K (c) 100K and (d) 2.8K. Arrow indicates the AFM peak. The vertical tick marks correspond to the position of all allowed Bragg reflections for the nuclear (top) and magnetic (bottom) reflections.

moment, listed in Table 3.5, are in good agreement with those reported in the literature [90]. The Rietveld refinement results confirm that both the nuclear structure with R3c space group and the magnetic structure do not change down to the lowest temperature as a result of the magnetic transitions. The fact that the AFM peak, marked with arrow in the figure, persists down to 2.8K clearly suggests that the LRO AFM phase coexists with the SG phases. We modelled the temperature dependence of the integrated intensity of the AFM peak using the molecular-field theory according to which the magnetic moment should follow the following temperature dependence [265],

$$\frac{\mu}{\mu_0} = B_J(x), \text{ where } x = \left( \frac{3J}{J+1} \frac{T_C}{T} \frac{\mu}{\mu_0} \right) \qquad \text{.....(3.8)}$$

Here, J is the total angular momentum of the system, $\mu/\mu_0$ is the ratio of the magnetic moment at temperature T to that at T= 0K, and $B_J$ is the Brillouin function

$$B_J(x) = \frac{2J+1}{2J} \coth\left( \frac{2J+1}{2J} x \right) - \frac{1}{2J} \coth\left( \frac{1}{2J} x \right) \qquad \text{.....(3.9)}$$

We fitted the square of the ordered magnetic moment to the experimentally measured integrated intensity of the AFM peak as a function of temperature and the results are shown in Fig. 3.23. Solid line in the figure is the fit for the square of the Brillouin function behaviour. Evidently, the observed variation of the integrated intensity of the AFM peak deviates from the molecular field behavior around the two SG transition temperatures. This decrease in the integrated intensity around $T_{SG1}$ and $T_{SG2}$ clearly suggests that some spin components are being removed from the LRO AFM phase regions and transformed to the glassy phase. This proves that the two SG phases are

Table 3.5: Refined nuclear and magnetic structural parameters and agreement factors using NPD data at 300K, 200K, 100K and 2.8K with R3c space group.

| **Parameters** | **NPD 300 K** | **NPD 200 K** | **NPD 100 K** | **NPD 2.8 K** |
|---|---|---|---|---|
| $a_{hex}$ (Å) | 5.6132 (5) | 5.6084 (5) | 5.6052 (5) | 5.6051 (4) |
| $c_{hex}$ (Å) | 13.9078 (2) | 13.8939 (1) | 13.8825 (1) | 13.8813 (1) |
| $v_{hex}$ (Å) | 379.42 (6) | 378.48 (6) | 377.73 (6) | 377.59 (5) |
| α, β, γ | $\alpha=\beta=90^0$, $\gamma=120^0$ | $\alpha=\beta=90^0$, $\gamma=120^0$ | $\alpha=\beta=90^0$, $\gamma=120^0$ | $\alpha=\beta=90^0$, $\gamma=120^0$ |
| Bi/Ba (z) | 0.2854 (5) | 0.2865 (4) | 0.2862 (4) | 0.2859 (4) |
| Fe/Ti (z) | 0.0110 (6) | 0.0119 (4) | 0.0110 (5) | 0.0115 (4) |
| O (x) | 0.2116 (8) | 0.2117 (6) | 0.2171 (6) | 0.2159 (6) |
| O (y) | 0.3468 (4) | 0.3466 (7) | 0.3488 (6) | 0.3487 (6) |
| O (z) | 1/12 | 1/12 | 1/12 | 1/12 |
| $\beta_{Bi/Ba}$(Å$^2$) | $\beta_{11}=\beta_{22}=2\beta_{12}$ = 0.0363 (2) $\beta_{33}$ = 0.0031 (3) | $\beta_{11}=\beta_{22}=2\beta_{12}$ = 0.0313 (2) $\beta_{33}$ = 0.0029 (4) | $\beta_{11}=\beta_{22}=2\beta_{12}$ = 0.0250 (2) $\beta_{33}$ = 0.0026 (3) | $\beta_{11}=\beta_{22}=2\beta_{12}$ = 0.031 (2) $\beta_{33}$ = 0.0024 (2) |
| $\beta_{Fe/Ti}$ (Å$^2$) | 1.33 (9) | 1.30 (5) | 1.27 (9) | 1.27 (8) |
| $\beta_O$(Å$^2$) | $\beta_{11}$= 0.057 (3) $\beta_{22}$ = 0.019 (1) $\beta_{33}$ = 0.002 (3) $\beta_{12}$ = 0.025 (2) $\beta_{13}$ = 0.003 (9) $\beta_{23}$ = 0.006 (4) | $\beta_{11}$= 0.048 (5) $\beta_{22}$ = 0.011 (3) $\beta_{33}$ = 0.002 (3) $\beta_{12}$ = 0.019 (7) $\beta_{13}$ = 0.003 (6) $\beta_{23}$ = 0.006 (5) | $\beta_{11}$= 0.039 (3) $\beta_{22}$ = 0.004 (13) $\beta_{33}$ = 0.003 (2) $\beta_{12}$ = 0.014 (2) $\beta_{13}$ = 0.002 (7) $\beta_{23}$ = 0.005 (3) | $\beta_{11}$= 0.046 (3) $\beta_{22}$ = 0.008 (14) $\beta_{33}$ = 0.003 (2) $\beta_{12}$ = 0.017 (1) $\beta_{13}$ = 0.004 (7) $\beta_{23}$ = 0.006 (4) |
| $\mu_{Fe}$ ($\mu_B$) | 3.25 (8) | 3.55 (7) | 3.75 (8) | 3.82 (7) |
| $R_{wp}$ (%) | 9.15 | 9.89 | 9.87 | 9.03 |
| $R_{mag}$ (%) | 4.63 | 4.21 | 3.39 | 3.36 |
| $\chi^2$ | 7.58 | 8.35 | 9.80 | 8.38 |

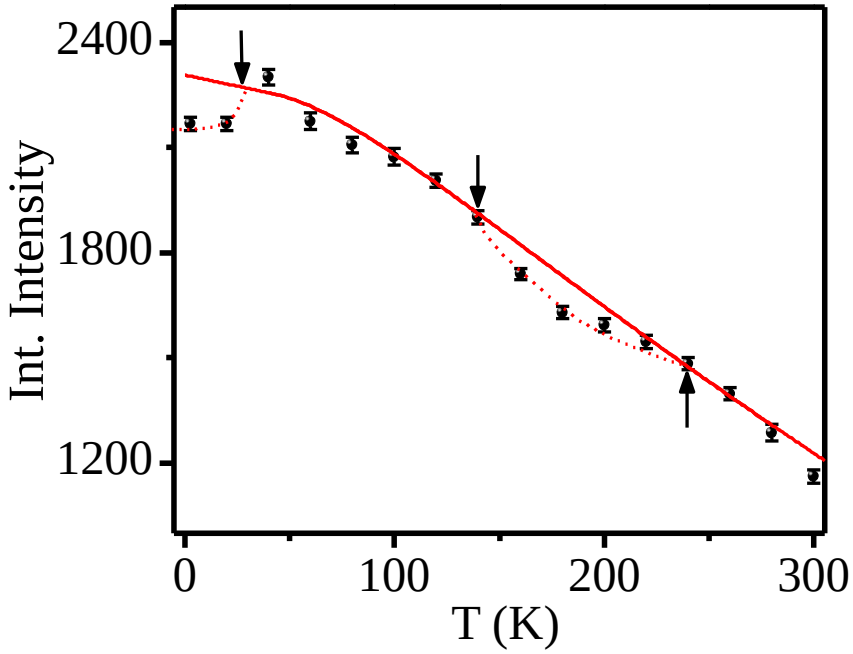


Figure 3.23: Temperature dependent variation of the integrated intensity of the AFM peak (111) of BF-0.20BT (The miller indices are with respect to a doubled pseudocubic cell). Solid line is fit for Brillouin function.

formed on the same magnetic sublattice [172] that gives rise to the LRO AFM phase and that they are not due to nanosized impurity phases, proposed in the context of the low temperature SG phase of pure $BiFeO_3$ [88,266,267] or smaller SPM clusters in a segregated magnetic microstructure proposed in the context of $Pb(Fe_{1/2}Nb_{1/2})O_3$ [171].

### 3.4.9 Evidence for isostructural phase transitions and polarization changes across the spin-glass transitions in BF-0.20BT:

Even though the space group symmetry of BF-0.20BT does not change in the 300 to 2.8K temperature range, the fractional coordinates of $z_{Bi/Ba}$ and $z_{Fe/Ti}$, obtained by Rietveld refinements using neutron diffraction data, change discontinuously around the two spin-glass transition temperatures as shown in Fig. 3.24. Further, the coordinates of the two oxygen positions ($x_O$ and $y_O$) show anomalies around the third transition driven by electromagnons. This change of atomic positions (fractional coordinates) can be explained in terms of one of the irreducible representations (Irrep) of the R3c space group corresponding to an optical phonon mode at k= (0,0,0) point of the Brillouin zone, as discussed in the supplemental information of Ref. [89]. Such a change of atomic positions

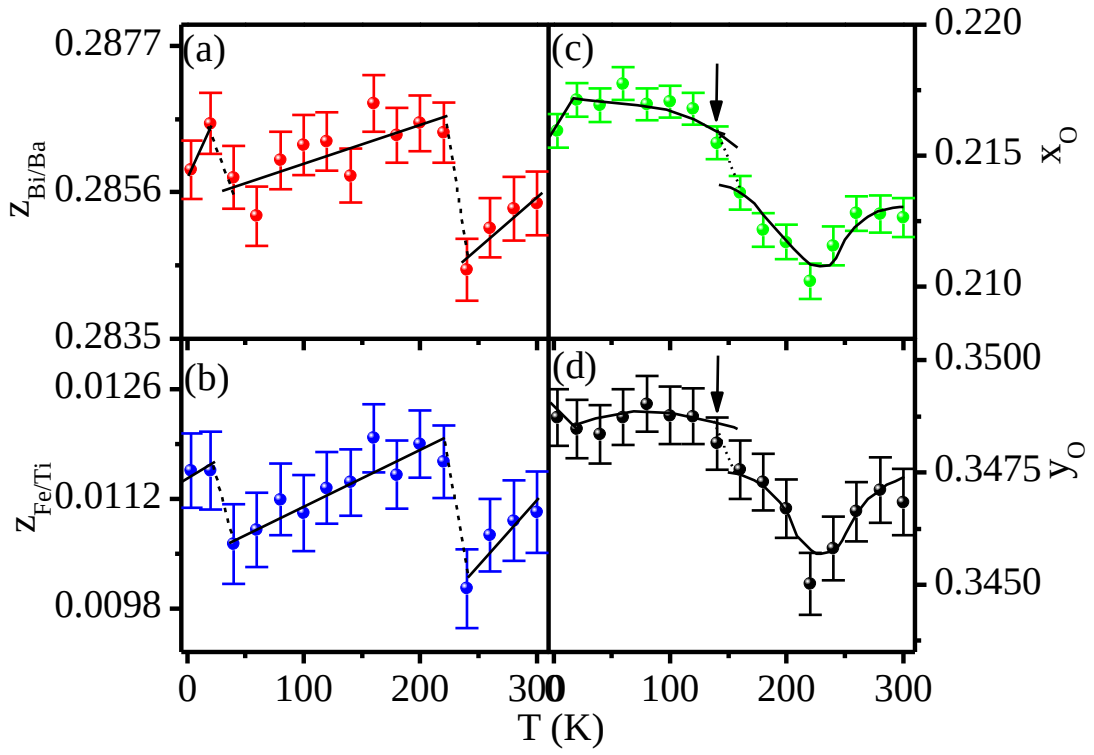


Figure 3.24: Temperature dependence of the fractional z coordinates of (a) Bi/Ba and (b) Fe/Ti. The x and y coordinates of O are shown in (c) and (d). All these coordinates were obtained from the Rietveld refinements using neutron powder diffraction data.

without any change in the space group symmetry has previously been observed in $BiFeO_3$ solid solutions across $T_N$ where it has been attributed to an isostructural phase transition (ISPT) [89,90,94]. We believe that the anomalies in atomic positions across the three low temperature magnetic transitions in BF-0.20BT are due to similar ISPTs driven by spin-polar phonon coupling (SPC). In literature [268], the origin of SPC effect has been attributed to the electronic structure which may suggest that the low temperature transitions in BF-0.20BT could be of electronic origin.

As a result of change in the atomic positions due to the ISPT, the ferroelectric polarisation ($P_s$) is known to change significantly by about 2 to 3 $\mu C/cm^2$ at $T_N$ revealing magnetoelectric coupling in $BiFeO_3$ solid solutions including BF-0.20BT [89,90,94].

We have also calculated $P_s$ below room temperature from Rietveld refined coordinates, unit cell parameters and first principles derived Born Effective Charges (BEC) taken from the literature [79] using the following relationship:

$$P = e/V \sum_k z'_k \Delta(k), \qquad \text{.....(3.10)}$$

where the sum runs over all the ions inside the unit cell while $\Delta(k)$ is the displacement of the $k^{th}$ ion from its ideal cubic perovskite position, $z'_k$ the Born effective charge for $k^{th}$ ion and V the volume of the primitive unit cell. The temperature variation of $P_s$ so obtained is shown in Fig. 3.25 which reveals distinct changes across the two SG transitions. The change in $P_s$ observed by us around $T_{SG1}$ and $T_{SG2}$ is (5±1)μC/cm$^2$ and (2±1)μC/cm$^2$, respectively, which are of similar order of magnitude as reported at the $T_N$ for BF-0.20BT [90]. The observation of large change in $P_s$ ($\Delta P_s$) at the two SG transitions not only reveals strong magnetoelectric coupling but also provides additional microscopic evidence for the coexistence of the SG and the LRO phases on the same magnetic sublattice at the two spin glass transition temperatures due to multiferroic nature of the two SG phases.

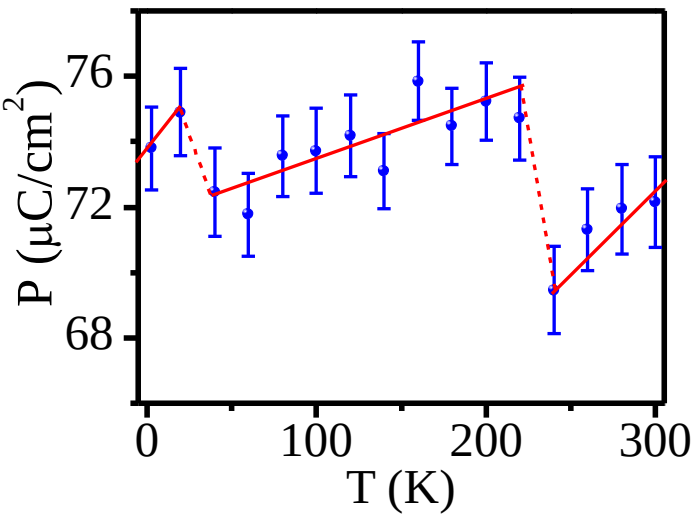


Figure 3.25: Temperature dependent variation of the spontaneous polarization calculated from the positional coordinates.

### 3.5. Magnetic phase diagram of BF-xBT:

In this section, we briefly discuss the effect of $BaTiO_3$ concentration (x) on the low temperature phase transitions of $BiFeO_3$ with the objective of constructing a magnetic phase diagram of BF-xBT system using the transition/freezing temperatures obtained from ZFC M(T) and AC susceptibility measurements (see Figs. 3.26-3.28). Fig. 3.26 depicts the plot of ZFC M(T) for various compositions (x). Signature of a transition to a LRO magnetic state is clearly seen upto x=0.40. For x=0.50 also, a diffuse transition is seen in the figure but for x = 0.60 there is no signature of this transition in the M(T) plot. Disorder induced gradual broadening of the transition is seen quite clearly in this figure for higher x values. The LRO transition temperature $T_N$ was determined from the first derivative of M(T) shown in Fig. 3.26(b). It shows clear dips for all the compositions including x = 0.50 due to the Néel transition (see also the inset of Fig.3.26(b)). The composition dependence of $T_N$ shown in Fig. 3.29 could be described using $(x-x_c)^n$ type dependence with n = 0.30±0.02 and $x_c$ = 0.55±0.01. In the previous neutron diffraction studies [91], AFM peak was observed for x = 0.50 but not for x=0.60 which also suggests that $x_c$ lies in the range $0.50 \leq x_c \leq 0.60$. We believe that $x_c$ = 0.55 is the percolation threshold limit for the LRO phase to emerge in the presence of disorder introduced by $BaTiO_3$ substitution in the $BiFeO_3$ matrix.

To investigate the effect of disorder (x) on the SG1 and SG2 transitions, we show in Fig. 3.27 the $\chi'$ ($\omega$, T) plots at 497.3 Hz for various compositions of BF-xBT. The variation of $\chi'$ ($\omega$, T) for x = 0.10, 0.20 and 0.30 are similar where the peaks corresponding to SG1 and SG2 transitions are clearly seen. While two peaks in the $\chi'$ ($\omega$, T) plot are also seen for x= 0.40, the magnitude of the susceptibility below the SG1 transition shows a slightly increasing trend with decreasing temperature whereas it shows a decreasing trend

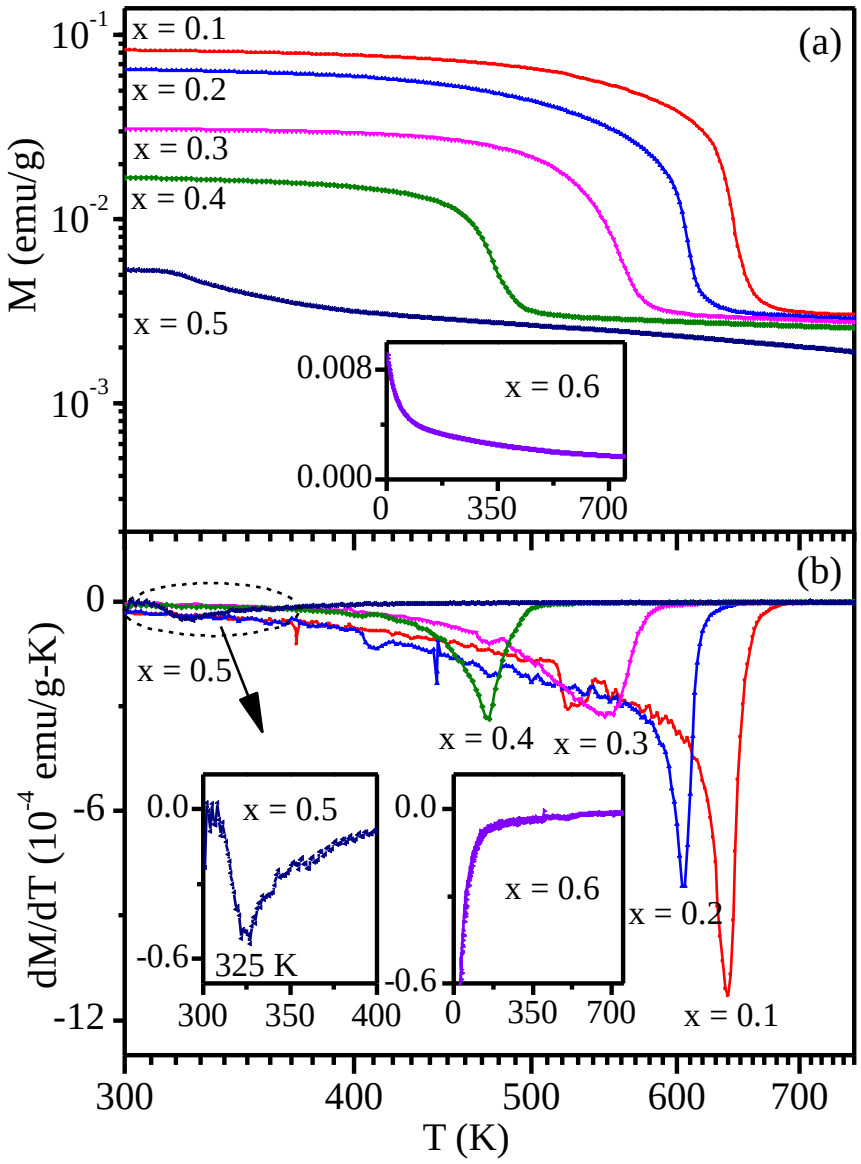


Figure 3.26: (a) The variation of ZFC magnetization with temperature measured at a field of 500 Oe for various compositions in the range $0.10 \leq x \leq 0.60$. (b) shows first derivative of M (dM/dT) with respect to temperature for these compositions.

for x = 0.10, 0.20 and 0.30 showing that the disorder affects the two transitions differently. For x= 0.50, only one peak corresponding to the SG2 transition is seen clearly. There is, however, an inflection point around 51K which could possibly be linked with the SG1 transition. The composition dependence of the SG1 and SG2 transition temperatures are shown in Fig. 3.29. The SG1 transition temperatures for various

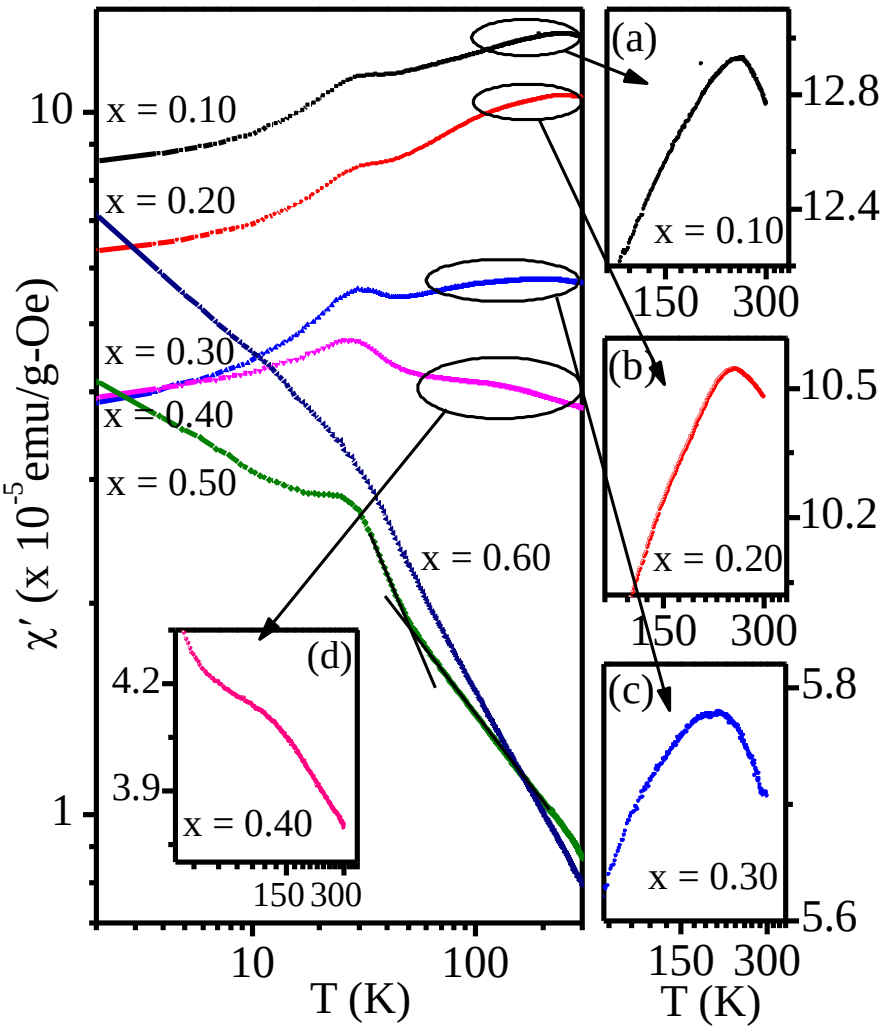


Figure 3.27: Left panel shows the variation of χ' (ω, T) of BF-xBT with temperature at 497.3 Hz frequency for various compositions in the range $0.10 \leq x \leq 0.60$. Right panel (a-c) as well as panel (d) depict the zoomed view around the SG1 transition.

compositions, including x= 0.40 and 0.50, also show $T_c \sim (x-x_c)^n$ type dependence with $x_c$ =0.55±0.01 but with an exponent n = 0.49±0.07. This exponent (n ~½) is reminiscent of a quantum phase transition [269,270] and the possibility of the existence of a quantum critical point corresponding to the percolation threshold composition $x_c$= 0.55 for the SG1 transition needs to be investigated carefully in a future work. Further, the extrapolation of the curve for SG1 transition to x = 0 predicts a transition around 260K for $BiFeO_3$.

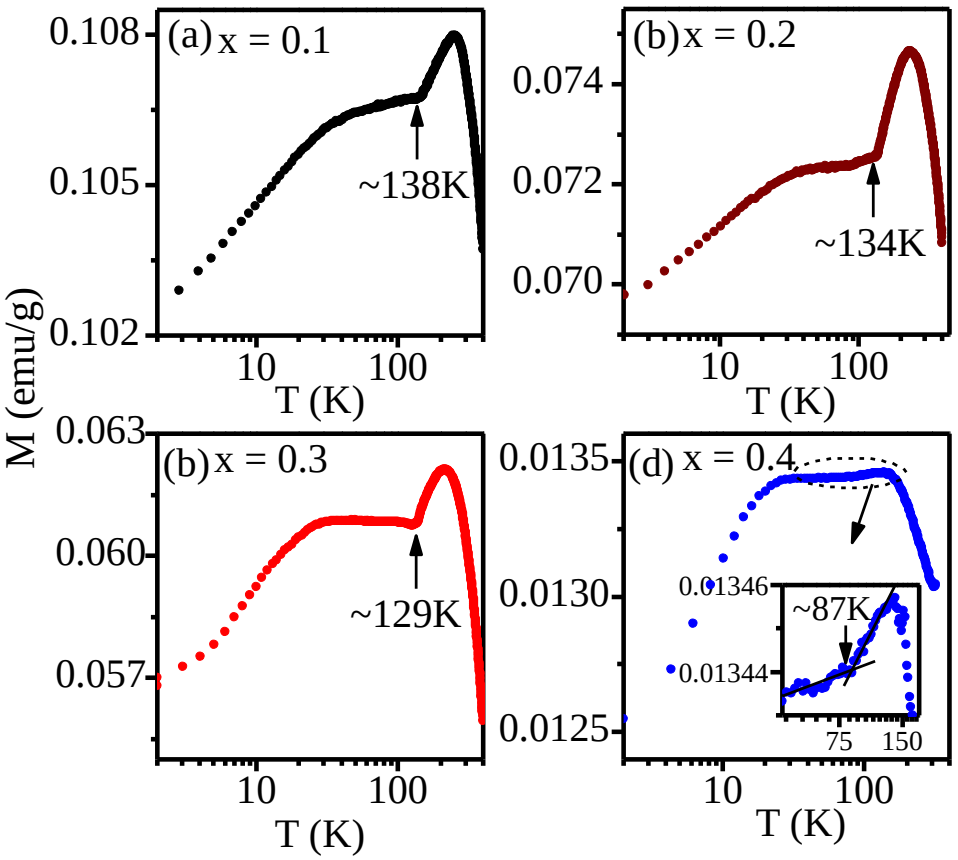


Figure 3.28: The variation of ZFC magnetization of BF-xBT with temperature below 300K measured at field of 500 Oe for compositions (a) x= 0.10, (b) x = 0.20, (c) x = 0.30 and (d) x = 0.40.

This transition was presented in the previous chapter. It is likely that this transition in $BiFeO_3$ may also have a spin glass character as predicted in the literature [103]. In contrast to the SG1 transition, the SG2 transition temperature shows weak composition dependence upto about x= 0.40 but significant decrease is seen for x=0.50. From the least squares fit to the observed $T_{f2}$ values using $(x-x_c)^n$ type dependence, the critical composition limit for this transition is also found to be close to $x_c$=0.55 but with an exponent n =0.08. We have also examined the composition dependence of the intermediate transition, that occurs between the SG1 and SG2 transitions and is known to be driven by electromagnons in pure $BiFeO_3$, using ZFC M(T) plot below room

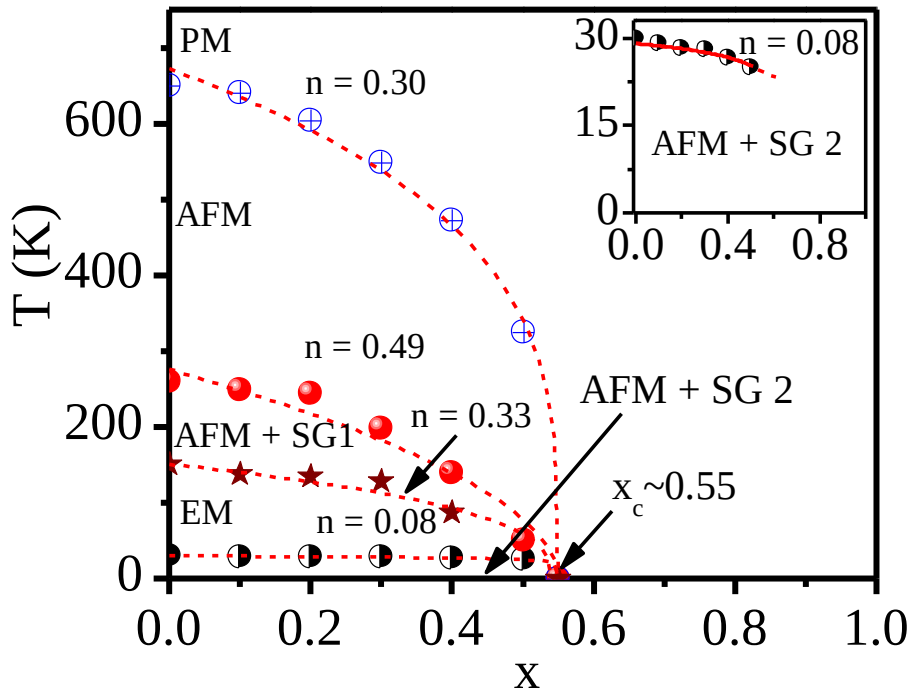


Figure 3.29: Phase diagram of BF-xBT. PM: Paramagnetic, SG: Spin glass, AFM: Antiferromagnetic, EM: Electromagnon. The SG2 transition temperatures (see the inset) shows the weakest composition dependence. The dotted lines through the data points depict the least squares fit for $T_c \sim (x-x_c)^n$ type dependence with $x_c$ = 0.55 giving n = 0.30, 0.49, 0.33 and 0.08 for the AFM, SG1, electromagnon driven and SG2 transitions, respectively. The exponent n ~ ½ indicates the possibility of a quantum critical point at $x_c \sim 0.55$.

temperature shown in Fig. 3.28 for four different compositions of BF-xBT. The M(T) plot shows a peak corresponding to the SG1 transition whereas the SG2 transition is signalled by a step like decrease in the magnetization value at low temperatures. As a result of dilution of the magnetic sublattice due to disorder, magnetization decreases and the peak corresponding to the SG1 transition becomes less prominent for x= 0.40. The electromagnon transition is signalled by a kink (for $x \leq 0.30$) or a dip (x=0.40) at the foothill of the SG1 peak. The corresponding transition temperature shows a rather weak composition dependence upto x= 0.30. The composition dependence of this transition temperature ($T_c$) was also fitted to $(x-x_c)^n$ type function which gave us n = 0.33±0.06 and $x_c$ = 0.55±0.02. The phase diagram presented in Fig. 3.29 clearly shows the SG1 and SG2

transitions as well as the intervening third transition supposedly driven by electromagnons for all the compositions with $x < x_c$. This intermediate transition was not envisaged in the existing theories of a succession of two spin-glass transitions in Heisenberg system [50–53] and needs to be looked into in a future work.

### 3.6. Conclusions:

Excellent quality samples of (1-x)$BiFeO_3$-x$BaTiO_3$ (BF-xBT) solid solutions with x = 0.10, 0.020, 0.30, 0.40, 0.50, and 0.60 were synthesized by the conventional solid state route and characterized by laboratory source and synchrotron based XRD, SEM, EDX and EPMA for their phase purity, crystal structure, microstructure and composition. The low temperature magnetic transitions were investigated using DC magnetization measurements as a function of temperature (M (T)), time (M(t)), field (M (H)) and sample history (ZFC and FC conditions), AC susceptibility measurements as a function of frequency (ω) and temperature (T) (χ (ω,T)), as well as low temperature XRD and neutron diffraction measurements.

We have presented evidence for two spin-glass transitions (SG1 and SG2) in the BF-xBT system using a series of bulk measurements revealing history dependent effect, critical slowing down of the spin dynamics due to ergodicity breaking, existence of A-T and G-T lines due to freezing of the longitudinal and transverse components of the spins and stretched exponential type decay of the thermoremanent magnetization. Using neutron and x-ray diffraction measurements, which provide evidence on microscopic scales, we have shown that the two spin-glass transitions are not only intrinsic to the BF-xBT system but also occur on the same magnetic sublattice in coexistence with the long range ordered antiferromagnetic phase. Our results show for the first time that the spontaneous polarization ($P_s$) and unit cell volume (V) show significant variation across the SG1 and SG2 transitions confirming the presence of magnetoelectric and

magnetoelastic couplings, respectively. These couplings, and possibly the presence of electromagnons, constitute unique features of a multiferroic spin-glass system like BF-xBT that distinguish it from the conventional spin glass systems. While the existence of the A-T and G-T lines confirms that the SG1 and SG2 transitions result from the freezing of the longitudinal and transverse components of spins, as predicted theoretically for Heisenberg systems with small single ion anisotropy (D), there are a few unexplained aspects of our observations. First and foremost is whether the smeared SG1 transition could have a structural origin, rather than magnetic. Although the SG1 transition is not found to be linked with any change in the space group symmetry, the occurrence of isostructural phase transition (ISPT) has been confirmed by us which indicates spin-phonon coupling. Secondly, the temperatures for the two spin-glass transitions are far too apart whereas the difference between the two-successive spin-glass transitions in conventional spin glasses is rather modest (<50K). Thirdly, the two spin-glass transitions are not successive as there is another transition, possibly driven by electromagnons, in between the two spin glass transitions. Any plausible theory of spin-glass transitions in a multiferroic system requires consideration of magnetoelastic and magnetoelectric couplings as well as electromagnons, if present. The mechanism of spin-phonon coupling (electronic or otherwise) needs to be investigated for each multiferroic system since it differs from compound to compound [268]. We hope that our results would stimulate future theoretical work to consider the effect of these couplings and electromagnons in the mean field theories as well as Monte Carlo simulation studies of SG transitions in insulating magnetoelectric multiferroics like $BiFeO_3$.